UNIVERSITY OF CALIFORNIA

RIVERSIDE

Experimental Investigation and Numerical Simulation of Smoke, Fire, and Biological Heat Transfer

A Thesis submitted in partial satisfaction
of the requirements for the degree of

Master of Science

in

Mechanical Engineering

by

Stephanie Minh Pham

December 2016

Thesis Committee:

Dr. Marko Princevac, Chairperson
Dr. Masaru Rao
Dr. Hideaki Tsutsui

The Thesis of Stephanie Minh Pham is approved:

_____

_____

_____

Committee Chairperson

University of California, Riverside

ACKNOWLEDGEMENTS

Most of all, I would like to acknowledge my advisor and mentor, Dr. Marko Princevac. I am honored to be given the opportunity to work in both the laboratory and classroom setting under him. Instructing and designing the course Ship Theory, since its inception, with him was a very rewarding and maturing experience. I am thankful for his high expectations and belief in my capabilities along with caring about my well-being 7and personal development. He has been a prime example of leadership and a role model. The lessons that I have learned from him will be carried throughout my career.

I wish to thank Dr. Masaru Rao for serving on my committee and enlightening me on current scientific research by hosting the seminar series my first year. I also wish to thank Dr. Hideaki Tsutsui for serving on my committee and giving me the opportunity of developing a design concept for his bioreactor project.

I would like to thank Dr. Jerome Schultz for choosing me to work under him for the heat transfer project. And I would like to acknowledge Dr. Trevor Maynard and Dr. Christian Bartolome because their work assisted me in moving my flame merging project forward.

I would like to give thanks to Dr. David Weise, Gloria Burke, and Joey Chong of the United States Department of Agriculture (USDA) Forest Service for their guidance and ensuring we perform our experiments safely. And I would like to acknowledge my Brazilian intern Carla Diaz and French interns Romain Bacq and Nicolas Fisichella for performing our experiments.

Lastly, I would like to thank my lab mates of the Laboratory for Environmental Flow Modeling, Jeanette Cobian, Ben Sommerkorn, and AmirHessam Aminfar, for advising and keeping me mentally stable during graduate school.

This is dedicated to my loving family for their support; especially to my mom, dad, and aunt. Thank you for all your prayers.

ABSTRACT OF THE THESIS

Experimental Investigation and Numerical Simulation of
Smoke, Fire, and Biological Heat Transfer
by

Stephanie Minh Pham

Master of Science, Graduate Program in Mechanical Engineering
University of California, Riverside, December 2016
Dr. Marko Princevac, Chairperon

This thesis documents three diverse projects done in the Laboratory for Environmental Flow Modeling. They are presented in the following order: 1) Interception of Smoke from a Forest Canopy, 2) Flame Merge Experiment, and 3) Examination of Testicular Thermoregulation. The first project is an experimental investigation of possible filtering of particulate matter from wildfire smoke dispersing upwards through forest trees of the canopy layer. If the filtering is significant, then it should be accounted for when modeling air quality impact, visibility, and other environmental effects of surface fires in forests. The second project is an experimental investigation of the processes of flame merging and tilting with no wind velocity. It was determined that the flame distance, fuel mass, flame size, and fuel bed configuration are the parameters that influence when the flame will "see" the other flame or obstacle. The third project is to further knowledge of thermoregulation processes of the testicle by examining the influence of cell metabolism and perfusion in tissue through numerical simulation. Detailed modeling of temperature field development inside the isolated and non-isolated testicle show negligible influence.

Table of Contents

List of Tables

List of Figures

1. Interception of Smoke from a Forest Canopy

1.1 Introduction

Smoke contains carbon monoxide, carbon dioxide, and microscopic solid and liquid particles (Auburn.edu n.d.). The size of these particles is directly related to the potential health problems they can cause. The small particles of concern are fine particles and inhalable coarse particles. Inhalable coarse particles are between sizes 2.5 and 10 micrometers ($PM_{2.5}$, PM_{10}), which can be inhaled to the lungs through the mouth and nostrils. Fine particles are of size $PM_{2.5}$ or less can get into eyes and travel into the blood stream following inhalation (AirNow 2003). Figure 1.1, taken from the Environmental Protection Agency (EPA)(US EPA 2012), shows the majority of $PM_{2.5}$ emissions found in our atmosphere comes predominantly from wildfire burns.

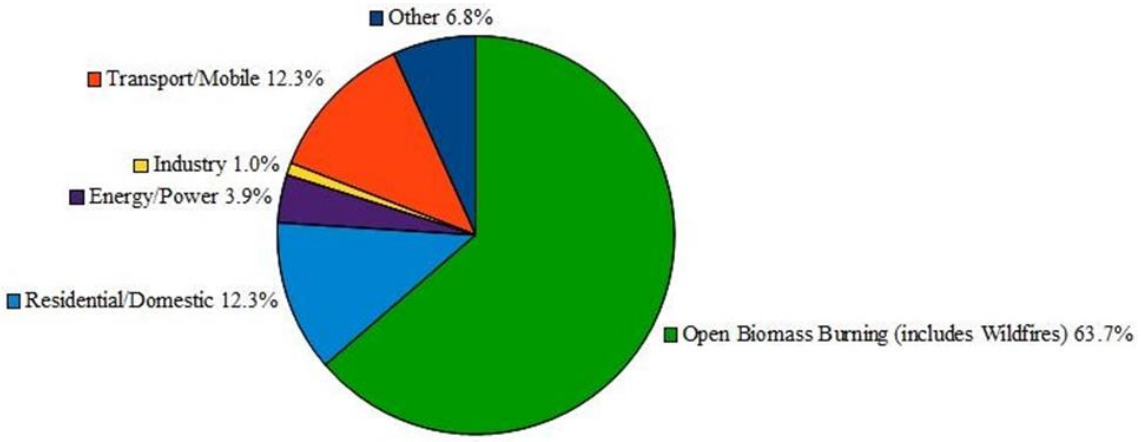

Figure 1.1 Contribution to $PM_{2.5}$ Emissions (US EPA 2012)

Solid and liquid particles from smoke can irritate eyes and airways, causing coughing, scratchy throat, irritated sinuses, headaches, stinging eyes or runny nose. Children, the elderly, and those suffering from heart and lung disease are primarily

sensitive to wildfire smoke. Children have underdeveloped respiratory systems and breathe in more air pollution per pound of body weight compared to healthy adults. The respiratory and cardiovascular systems of the elderly are weak due to age, making them more prone to heart and lung disease from pollutant inhalation. Furthermore, people suffering from heart and lung disease are more sensitive to smoke at a lower density. Those with heart disease may experience symptoms such as chest pains, palpitations, shortness of breath, or fatigue, while those suffering from lung disease may not breathe as deeply or as vigorously when pollutants are present in the air. Lung disease symptoms from smoke include coughing, phlegm, chest discomfort, wheezing, and shortness of breath. But even healthy young adults can experience health problems when smoke levels are beyond a certain threshold (AirNow 2003). If noxious plants such as poison ivy burn, smoke can cause skin rashes that can be more widespread on the body than those from direct contact with the plants (Auburn.edu n.d.).

Wildfire smoke can also cause visibility impairment. Superfog is the extreme condition of increased fog density associated with specific atmospheric and weather conditions. It is hypothesized that superfog forms when a considerable amount of water vapor is emitted from combustion of moist fuel during the smoldering phase of a wildfire at night time. When these water vapors mix with cold air under the right temperature and relative humidity conditions, the cold air becomes saturated and fog forms. Particulate matter from these smoldering fuels provides additional cloud condensation nuclei for the water vapor in the smoke; the resulting small droplets scatter light and visibility more effectively than regular fog. It has resulted in multiple tragic motor vehicle accidents as

visibility is typically less than three meters. In January 9, 2008, on the I-4 in Polk County Florida, a superfog event resulting from a nearby prescribed fire caused a 70-car pileup, which resulted in 5 fatalities and 38 injuries. In January 2012 a superfog event formed with smoke from a nearby wildfire on the I-75 near Gainesville, FL. The pileup included 7 semi-trucks and 12 cars claiming 10 lives and left 21 injured (Bartolome 2014).

Wildfire smoke can disperse far and settle into wilderness areas, causing environmental damage. Rainwater leaches inorganic nutrients and other materials from settled pollutants and dissolves them into adjacent soil, lakes, and streams, causing changes in its nutritional and chemical makeup. Decreases in water quality can be lethal to fish and other underwater inhabitants (Auburn.edu n.d.).

More than half of the most damaging fires in the U.S. of the past 170 years, has occurred in California (Fried, Torn, and Mills 2000). In southern California, fires are common in the hot and dry weather conditions of late summer and early fall because of "Santa Ana" winds (Florsheim 1991). Records of paleoclimatology and historical data show a correlation between increase in wildfire frequency and climate change, causing areas like southern California to be more susceptible to the detrimental effects on air quality, health, visibility, and land quality from smoke

In order to begin investigations on emission reduction, we start by creating a model. The aim of this project is to determine whether the concentration of emissions from wildfire smoke is being filtered through trees of the canopy layer. Experiments were

done with pine needles to aid in modeling the dispersion of emissions using the Gaussian Dispersion model found in Figure 1.2. The equation for this model can be written as

$$C = \frac{Q}{u}\frac{f}{\sigma_y\sqrt{2\pi}}\frac{g_1 + g_2 + g_3}{\sigma_z\sqrt{2\pi}} \qquad 1.1$$

where C is the concentration of emissions, Q is the source pollutant emission rate (g/s), u is the horizontal wind velocity, f is the crosswind dispersion parameter, σ_y and σ_z are the standard deviations of the distribution in the horizontal and vertical directions, respectively, and g_1+g_2+g_3 are the vertical parameters. The vertical parameters are expressed in the following equations:

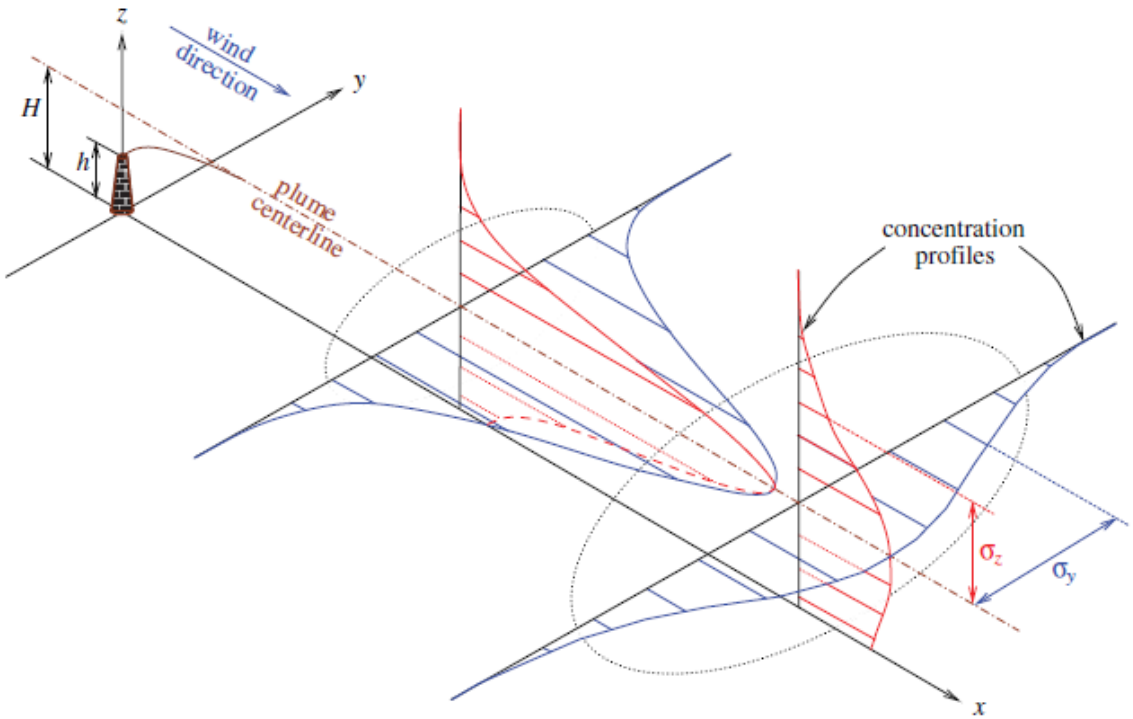

Figure 1.2 Visualization of the Gaussian Dispersion model (Stockie 2011)

$$g_1 = exp\left[\frac{-(z-H)^2}{2\sigma_z^2}\right] \quad 1.2$$

$$g_2 = exp\left[\frac{-(z+H)^2}{2\sigma_z^2}\right] \quad 1.3$$

$$g_3 = exp\left[\frac{-(z-H-2mL)^2}{2\sigma_z^2}\right] + exp\left[\frac{-(z+H+2mL)^2}{2\sigma_z^2}\right] + exp\left[\frac{-(z+H-2mL)^2}{2\sigma_z^2}\right] + exp\left[\frac{-(z-H+2mL)^2}{2\sigma_z^2}\right] \quad 1.4$$

Where H is the height of the emission plume centerline above ground level, L is the height from ground level to bottom of the inversion aloft, g_1 is the vertical dispersion with no image reflection and g_2 is the vertical dispersion for reflection from the ground. In real atmospheric conditions, dispersion in the upward direction is limited by the height of the atmospheric boundary layer; g_3 is the vertical dispersion for reflection from an inversion aloft (Stockie 2011).

In order to obtain the concentration of emissions, the source pollutant emission rate, Q, first needs to be determined; the other variables are dependent on position and velocity. The EPA fire emission model (Larkin and Raffuse 2015) is assessed to determine Q. The fire emission model is a function of fuel species as follows:

$$E(s) = A \cdot AFL \cdot \beta \cdot Ef(s) \quad 1.5$$

Where *A* is the area burned, which is determined by the burn scar of the environment. Other fires near the burn scar at the time are also researched in case of possible travelling. *AFL* is the available fuel load (wood, soil, grass) to burn. The term β is the fraction of available fuel consumed or the consumption efficiency, which is a function of fuel moisture, weather, and land type. Finally, *Ef(s)* is the emission factor of specific pollutants from fuel species, *s*, and is defined as mass of released pollutant per mass of burnt fuel with common units of g/kg or μg/kg (Larkin and Raffuse 2015). Figure 1.3 presents a typical experimental setup to determine the emission factor of a species. A known amount of fuel is burned and the mass of pollutant is measured from ignition to smoldering through a particle concentration measuring apparatus above the burning load.

Fuel consumption, *Fc*, is defined as the mass of fuel per seconds with units of kg/s. In Figure 1.3, we see an experimental set up with which fuel consumption can be determined by a known amount of fuel burned and timed from ignition to smoldering.

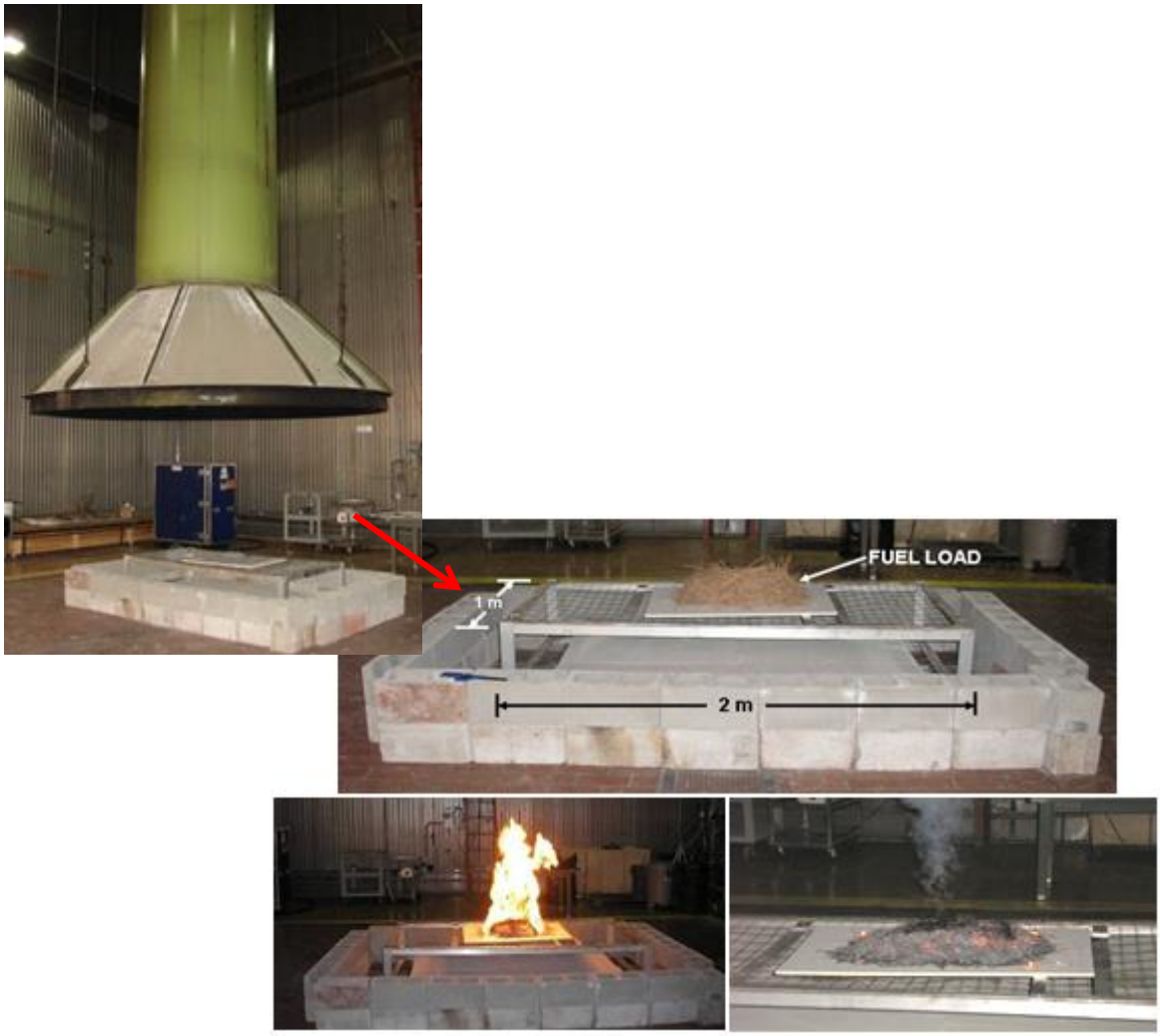

Figure 1.3 Emission Factor an Fuel Consumption experiment (USDA Forest Service Missoula Lab)

When fuel consumption and emission factors are known, the emission rate, *Q*, can be determined (Equation 1.6).

$$Q = Ef(s) \cdot Fc \qquad 1.6$$

Trees of the canopy layer are above the understory/shrub layer and forest floor and below the emergent layer in the forest structure, as shown in Figure 1.4. Tree canopies can grow up to 30 meters (rainforest) above the ground, have 3 to 12 meters in

thickness, and intercept about 95% of sunlight and precipitation. The ecosystem below is impacted through its ability to filter light. Leaves in the understory layer usually grow large due to the little sunlight and very few plants grow in the forest floor because of the scarcity of sunlight at this level (R. Butler 2015).

The objective of this project is to determine if trees of the canopy layer, as diagrammed in Figure 1.5, filter wildfire emissions of $PM_{2.5}$ from dispersing upwards. The hypothesis is as follows: as the canopy trees can filter light, they are similarly able to filter smoke, and by extension, reduce the emission factor. Should this be the case, we expect to be able to account for this reduction when modeling the impact air quality, visibility, and other environmental effects of surface fires in forests.

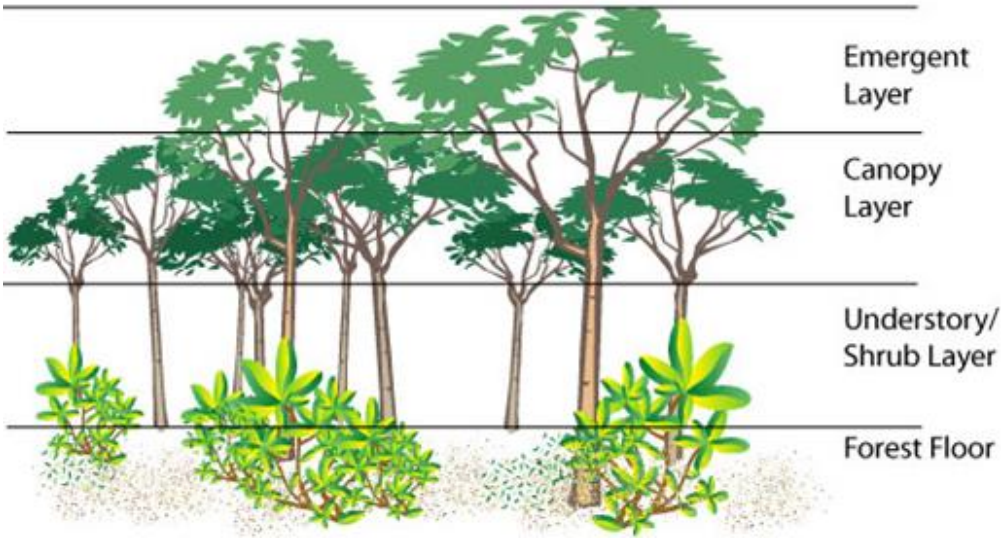

Figure 1.4 Canopy Tree forest Structure taken from Canopy Craze

We propose a factor, referred as Steph factor, *SF*, to be applied to the EPA fire emission model (Equation 1.5) for when canopy trees are present (Equation 1.7).

$$E(s) = A \cdot AFL \cdot \beta \cdot Ef(s) \cdot SF \qquad 1.7$$

Figure 1.5 Project Objective Picture (Ours 2015)

1.2 Experimental Setup

The "Interception of Smoke by a Forest Canopy" project runs at the University of California, Riverside's College of Engineering Center for Environmental Research and Technology (CE-CERT) facility and is a collaborative effort with the Forest Service, Environmental and Mechanical Engineering department.

The experimental setup consists of a rectangular duct, with one end above the fire, while the other end is equipped with a fan for flow control, as seen in Figure 1.6. The entire setup is placed in a two-story building. The fuel is burnt on ground level while smoke travels through the duct system to the top level where data acquisition is taken place.

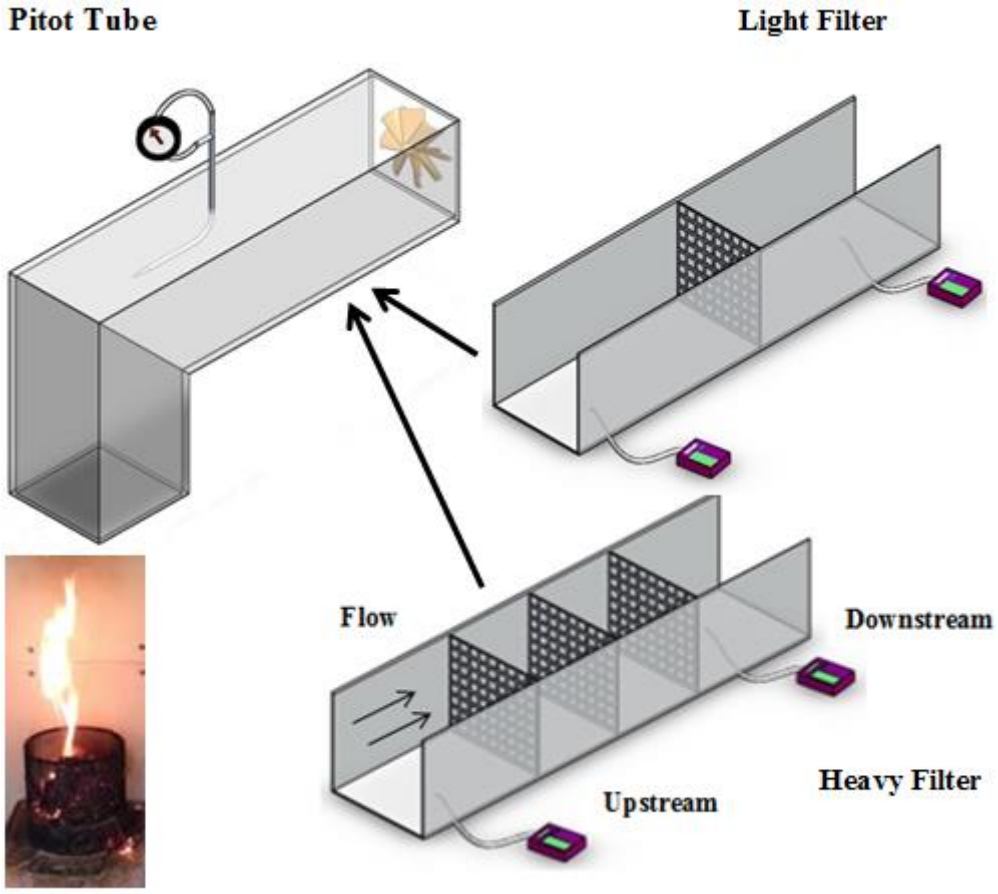

Figure 1.6 Duct system setup where data acquisition is taken place, fuel burning apparatus and position, and pitot tube placement to measure flow (left), Light Filter (top right), and Heavy Filter schematic with DustTrak Position (bottom center)

The Forest Service provided dried long-leaf pine needles as fuel and live Canary Island (*Pinus canariensis*) pine needles as filters. The emission factor of $PM_{2.5}$ for pine

needles was determined to be 21 g/kg (Robertson, Hsieh, and Bugna 2014), while fuel consumption and *SF* are determined experimentally. Live pine needles flattened between thin metal wire screens are used as a filter and placed in the duct to intercept flow. The screens cross sectional dimensions are 29 cm x 28 cm, while depth varied from 0.7 cm to 2 cm resulting in an averaged volume of approximately 1130 cm^3. For documentation purposes, photographs were taken of every filter with light shining on it and another with a back light for an idea of how particles pass though the filter. A photograph of a typical screen with live pine needles is given in Figure 1.7.

Figure 1.7 (Right) Filter characteristic documentation (Left) Filter flow conceptualization

Typically, 500 grams of dried pine needles were evenly fed into the circular fuel burning apparatus (Figure 1.6) over the course of 5 minutes. The burns were organized into "blocks," with each block consisting of one control burn (no filter), one light filter burn, and one heavy filter burn (Figure 1.6). In light filter burns, one filter screen is placed to intercept flow, while in heavy filter burns, three equally spaced screens are

placed into the test section. A total of nine blocks, twenty-seven burns, have been done. Block 3 was repeated for experimental accuracy (Table 1.1). Pitot tubes were used to determine the air flow characteristics in the duct (Figure 1.6). The flow speed was 6 m/s, which corresponds to the turbulent Reynold's number of 1.2×10^5. DustTrak sensors were used for particle concentration measurements in the smoke. Figure 1.6 shows the sensor positions with one placed upstream and one downstream of the filters.

1.3 Data Analysis

Image processing was used to determine permeability of the filters. Original images (Figure 1.7) were cropped to the highlighted green lines in Figure 1.8. The cropped images were converted to grayscale using MatLab and their histograms (Figure 1.9) were used to determine flow blocking and empty spaces of the filters. In the case of Figure 1.9, pixels with intensity range 0 to 180 (8-bit data with a total range of 0-255) are considered to be the blocking region and pixels with intensity range from 181 to 255 are considered to be empty space. This analysis was done for all filter images (Table 1.1) and was used to determine permeability by the ratio of empty region pixels to the total number of pixels. The filters had an average permeability of 20% with a standard deviation of 4%.

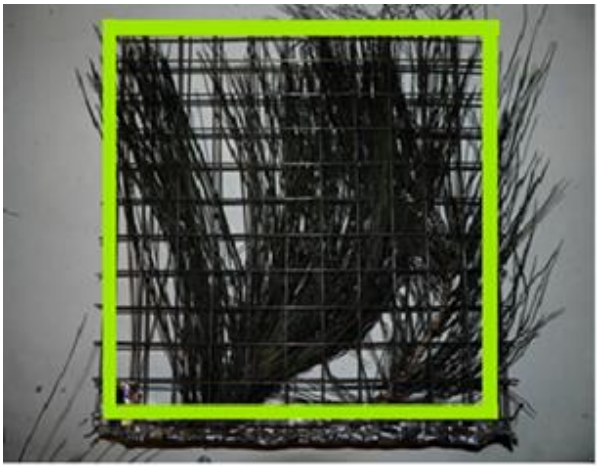

Figure 1.8 Sample of filter photograph taken by Forest Service, green box represents where the image is cropped

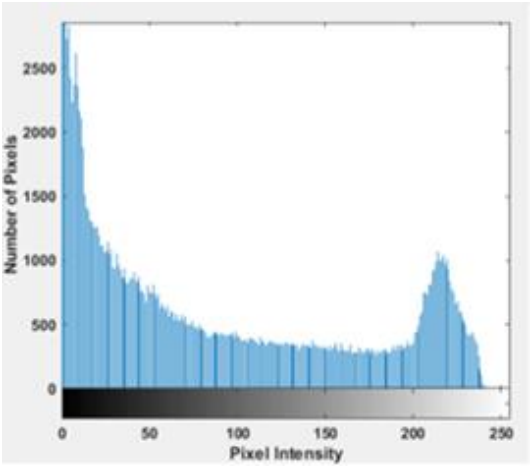

Figure 1.9 Histogram of pixel intensity for filter photograph

Table 1.1 Block Organization and Image Processing Data

Block #	Burn #	Light/Heavy/Control	% Permeability
Block 1	1	Control	100
	2	Heavy	29
	2	Heavy	24
	2	Heavy	26
	3	Light	31
Block 2	4	Heavy	21
	4	Heavy	22
	4	Heavy	19
	5	Light	23
	6	Control	100
Block 3a	7a	Heavy	25
	7a	Heavy	21
	7a	Heavy	22
	8a	Light	20
	9a	Control	100
Block 4	10	Light	20
	11	Heavy	25
	11	Heavy	25
	11	Heavy	25
	12	Control	100
Block 5	13a	Control	100

	13b	Control	100
	14	Light	16
	15	Heavy	24
	15	Heavy	19
	15	Heavy	22
Block 6	16	Light	17
	17	Heavy	12
	17	Heavy	15
	17	Heavy	23
	18	Control	100
Block 7	19	Heavy	12
	19	Heavy	17
	19	Heavy	18
	20	Light	14
	21	Control	100
Block 8	22	Heavy	19
	22	Heavy	17
	22	Heavy	15
	23	Light	19
	24	Control	100
Block 9	25	Light	18
	26	Control	100
	27	Heavy	17
	27	Heavy	14
	27	Heavy	21
Block 3B	7B	Heavy	22
	7B	Heavy	19
	7B	Heavy	20
	8b	Light	25
	9b	Control	100

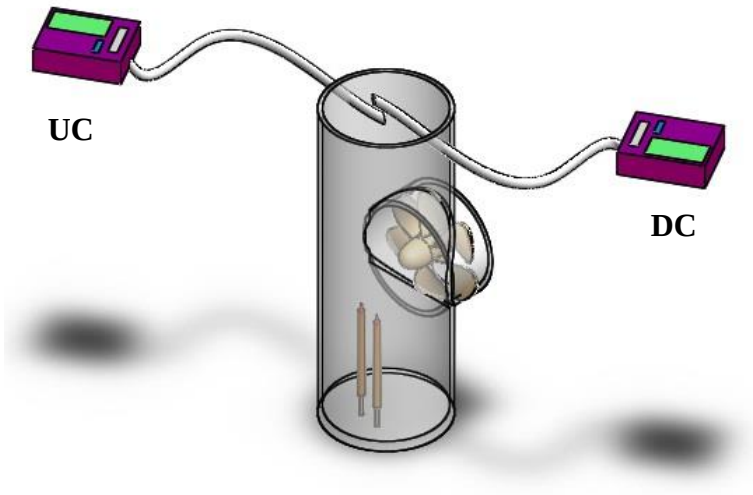

Figure 1.10 DustTrak Incense Smoke Calibration and DustTrak sensor labeling

The DustTrak sensors were labeled UC and DC for upstream concentration and downstream concentration, respectively. To assure consistent reading from all sensors, a separate calibration experiment was performed with incense smoke, as shown in Figure 1.10. Using a simple piping system to encompass smoke and fan to create the turbulence in the duct, the sensor's sampling tubes were placed side by side to determine whether they produced the same readings. It was observed that DC sensor consistently read higher values. We then concluded that the reading difference was a constant percent offset. Based on this difference, we devised a correction factor (Equation 1.8) to make readings from both sensors the same.

$$CF = \frac{A_{DC} - A_{UC}}{A_{UCDC}} \qquad 1.8$$

Here, A_{DC} and A_{UC} are the average readings of DC and UC DustTrak sensors, respectively. The denominator of Equation 1.8 is the average of both sensors, A_{UCDC} =

(A_{DC}+A_{UC})/2. This correction factor was used to calculate the corrected downstream concentration (C_{DC}) using the following equation:

$$C_{DC} = O_{DC} - (O_{DC} \cdot CF) \quad 1.9$$

The original DC, O_{DC}, is subtracted from the product of *CF* and $O_{DC.}$ These corrected values resulted in negligible concentration differences between the two. In Table 1.2, column three shows the difference between average C_{DC} and A_{UC}. Block 5 and 9 were removed for experimental accuracy.

The DustTrak data UC (blue) and both the O_{DC} (red) and C_{DC} (green) for Block 1 is plotted below. The peaks in Figures 1.11 to 1.13 correspond to the addition of fuel followed by the smoldering phase of the burn. Data for Figure 1.11 is the control burn, with no filter present. Figures 1.12 and 1.13 present measurements for light and heavy filter configurations, respectively. When the filters are present it can be seen that at certain peaks the O_{DC} is almost as much and at times more than upstream. The C_{DC} plot is less than upstream because of the application of the *CF*. The difference between C_{DC} and UC is greater when using heavy filters rather than light filters. The average percent difference was calculated for all light and heavy filters using the upstream and C_{DC} measurements. For light filters this difference is was found to be 14.4% and for heavy filters it is approximately 15%

Table 1.2 DustTrak Data

Block #	C/L/H	Average Difference
Block 1	C	-0.04
	H	-0.34
	L	-0.24
Block 2	C	-0.07
	H	-0.74
	L	-0.42
Block 3	C	-0.38
	H	-1.22
	L	-0.17
Block 4	C	0.06
	L	0.38
	H	0.11
Block 6	C	0.09
	L	0.32
	H	0.93
Block 7	C	0.04
	L	0.72
	H	0.41
Block 8	C	0.03
	H	0.36
	L	0.36

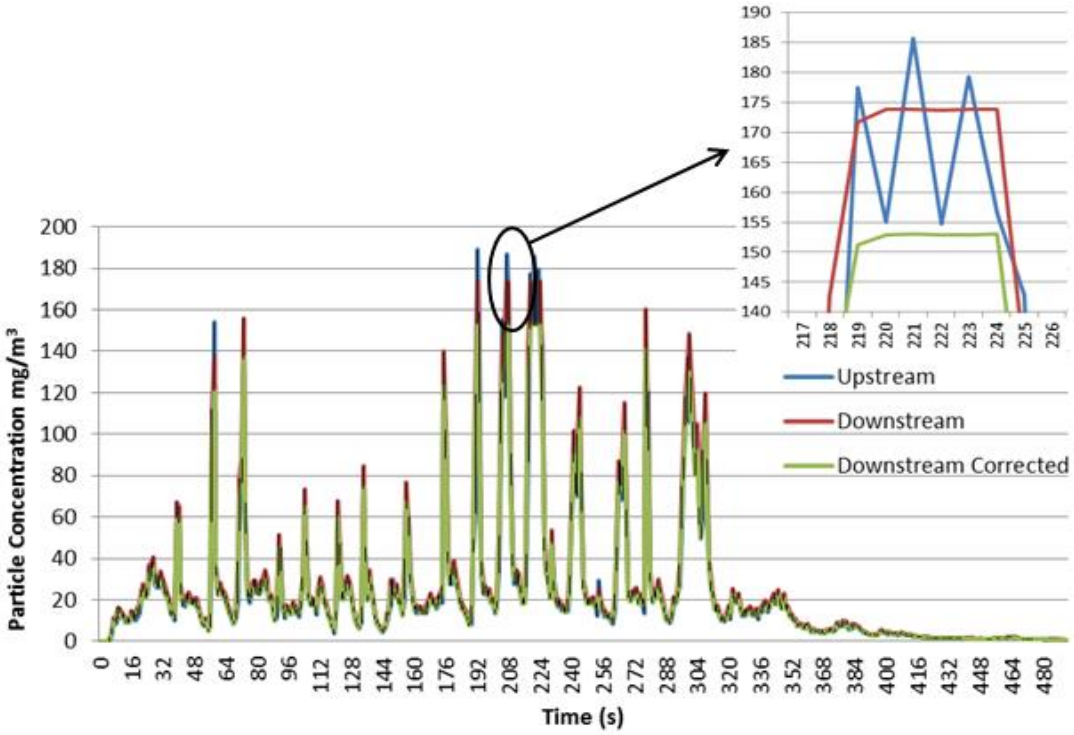

Figure 1.11 DustTrak Data Block 1 Control

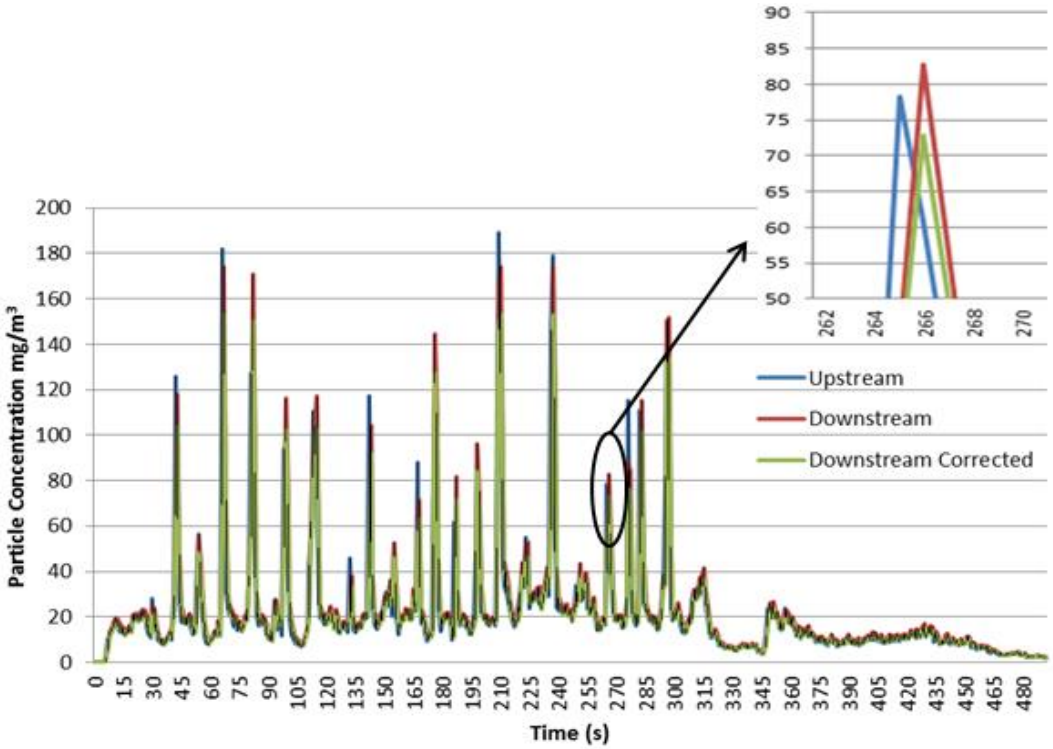

Figure 1.12 DustTrak Data Block 1 Light Filter

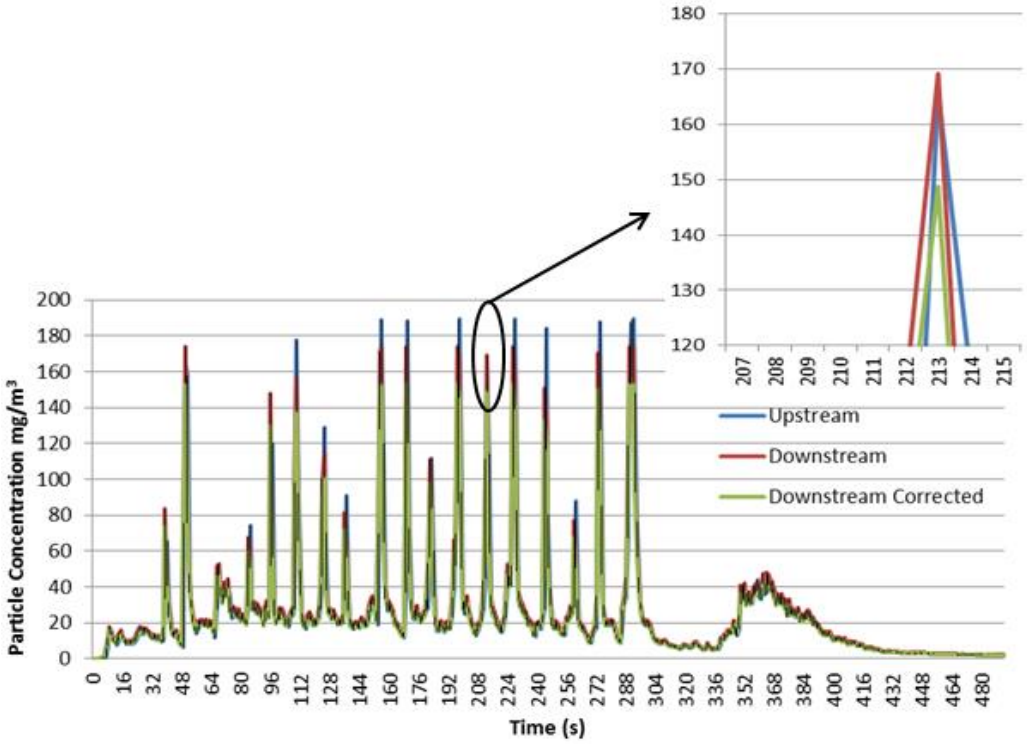

Figure 1.13 DustTrak Data Block 1 Heavy Filter

1.4 Conclusion

It was observed that the difference between down and upstream concentrations was not very significant, even for the case of heavy filters. There are several possible explanations for this. One possibility is that while the smoke passes through filters, the moisture within the filters condenses so that the downstream DustTrak detects water droplets as additional $PM_{2.5}$. Another possibility is that soot which had accumulated around the duct and on the filters were breaking away and travelling downstream. To test this possibility, an experiment was performed with natural gas as fuel instead of dried pine needles in order to observe whether heat was causing soot to dispatch. From this experiment, there was almost no difference between the DustTrak readings, which disproves this speculation. The third possibility is that the flow through the duct is too

high to realistically model updrafts through the canopy. Unfortunately, a reduction in the fan flow rate was not feasible, and a design involving the installation of a parallel duct to effectively reduce the flow through the filter screens was investigated, but was not implemented during the duration of the project. It is also possible that the canopy does not effectively filter $PM_{2.5}$, but this cannot be investigated further until the model has been further refined.

1.5 References

AirNow. May 2003. https://www.airnow.gov/index.cfm?action=smoke.index (accessed July 20, 2016).

Alan Long, Joshua Weiss, Marko Princevac, Christian Bartolome. "Superfog: State of the Science." *Southern Fire Exchange*, 2013.

Auburn.edu. n.d. http://www.auburn.edu/academic/forestry_wildlife/fire/effects.htm (accessed July 21, 2016).

Bartolome, Christian. 2014. "Electronic Theses and Dissertations UC Riverside Formation of Superfog from Wildland Fires – Theoretical and Physical Modeling A Dissertation Submitted in Partial Satisfaction of the Requirements for the Degree of Doctor of Philosophy in Mechanical Engine."

Butler, Rhet. *mongabay.com.* December 5, 2015. http://kids.mongabay.com/elementary/004.html (accessed July 20, 2016).

Butler, Rhett. *Mongabay.com.* July 30, 2012. http://rainforests.mongabay.com/0404.htm (accessed July 20, 2016).

Department of Health. September 2015. https://www.health.ny.gov/environmental/outdoors/air/smoke_from_fire.htm (accessed July 21, 2016).

Dorfman, Lynne, and Rose Capelli. *Canopy Craze.* n.d. http://588nonfictionguide.weebly.com/writing-activities.html (accessed July 21, 2016).

Florsheim, Joan L. 1991. "Fluvial Sediment Transport in Response to Moderate Storm Flows Following Chaparral Wildfire , Ventura County , Southern California," no. April: 504–11.

Fried, Jeremy S, Margaret S Torn, and Evan Mills. 2000. "The Impact of Climate Change on the Wildfire Severity: A regional Forcast for Northern California," 169–91.

Grenoble, Ryan. *huffingtonpost.com.* May 02, 2016. http://www.huffingtonpost.com/entry/wildfire-season-forecast-2016_us_57279d0ce4b0f309baf17c2d (accessed June 15, 2016).

Larkin, Sim, and Sean Raffuse. 2015. "Emissions Processing – Details Outline • How Do We Compute Emissions ? – Area Burned , Available Fuel Loading ,." In . San

Diego. https://www.epa.gov/sites/production/files/2015-09/documents/emissions_processing_details.pdf.

NGA's Learning Garden. 1999. http://garden.org/courseweb/course1/week4/page5a.htm (accessed July 20, 2016).

Ours, Laura. *UMD Right Now.* September 18, 2015. http://umdrightnow.umd.edu/news/umd-forest-mapping-instrument-space-station-passes-major-milestone (accessed July 21, 2016).

Robertson, Kevin M., Yuch P. Hsieh, and Glynnis C. Bugna. 2014. "Fire Environment Effects on Particulate Matter Emission Factors in Southeastern U.S. Pine-Grasslands." *Atmospheric Environment* 99. Elsevier Ltd: 104–11. doi:10.1016/j.atmosenv.2014.09.058.

Stockie, John M. 2011. "The Mathematics of Atmospheric Dispersion Modeling." *SIAM Review* 53 (2): 349–72. doi:10.1137/10080991X.

US EPA. 2012. "Chapter 4: Emissions of Black Carbon." *Report to Congress*. https://www3.epa.gov/blackcarbon/2012report/Chapter4.pdf.

2. Flame Merge Experiment

2.1 Introduction

Fire has played the role of two extremes since the beginning of civilization. It has been significant in mankind's advancement through benefits such as warmth, sterilization, and aiding in ecological biodiversity, but it has also been the cause of injuries, fatalities, and destruction.

Though there have been many studies on fire, there are still many deficiencies in our scientific knowledge of it. This is especially apparent when we look at the research that has been done in dynamic fire interactions. Finney claims, "A fundamental theory of wildland fire spread is missing." It is the intent of fire researchers to minimize the negative impacts of fire, but it is necessary to first develop a strong fundamental understanding. There have been efforts to model fire; however, the models of fire do not share a common formulation of the physical and chemical processes as they influence fire spread. Current models of wildland fire have a great deal of uncertainty, imprecision, and scarcity of input measurements. It was revealed, from investigation of these models, that most of the fundamentals were largely assumed without a sound experimental basis. Fire is a phenomenon, and Finney expresses that in order to understand it, it is important that we "(1) sufficiently understand its processes, (2) that we can adequately measure the conditions that influence those processes and (3) that the phenomenon's behaviour is uniquely the result of the measured conditions (Finney et al. 2013)."

Fire needs oxygen, heat, and fuel to propagate; when fire is active it entrains air in order to persist. Nelson, Butler, and Weise (Nelson, Butler, and Weise 2012) argue that

previous research has essentially neglected the processes governing movement of air into flame. They proceed to describe three cases of flame air entrainment; classical entrainment, dynamic entrainment, and accretive entrainment. In classical entrainment, it was hypothesized that in the absence of wind speed, the mass of entrained air increases as flame height increases, and the velocity of this air is proportional to the upward velocity of the flame. Dynamic entrainment occurs when wind speed is applied and convection begins to influence entrainment. Flame tilt is determined by a momentum flux balance between the transverse components of the horizontally moving ambient air and the vertical buoyant component of flame. Dynamic entrainment is associated with the flame's drag and buoyancy forces. Accretive entrainment occurs when the wind speed increases, and the mass of air entering the flame disrupts the balance between flame drag and buoyancy forces. The tilt angle is determined by the ratio of horizontal and vertical components of the flame mass flux.

There have been several experiments investigating both the dynamic and accretive entrainment cases for wildfire spread. Nelson, Butler, and Weise (Nelson, Butler, and Weise 2012) investigated the flame characteristics of 22 wind-aided fires in a laboratory wind tunnel, Weise and Biging (Weise and Biging 1986) studied flame length and angle with the combined effects of wind velocity and slope, and Albini (Albini 1981) modeled wind-blown turbulent flames from a line fire. Few experiments, however, were done in the classical entrainment case to understand how fire would interact, tilt, and spread in the absence of an external force. Maynard (Maynard 2013), investigated the flame tilting angle through line fires using Particle Image Velocimetry and used colored smoke

cartridges to visualize the entrainment. Jo did research on the behavior of the fire plume ejecting from an opening in vicinity of opposing walls to understand fire interaction with nearby obstacles (Jo et al. 2007). The objective of this project is to further the knowledge of classical entrainment by determining the critical distance of two fires for flame merging and tilting.

It is hypothesized that flame tilting between fires or fire and obstacle is primarily a function of distance. As two fires tilt or "see" each other, the air flow between the fire and the neighboring flame is restricted, resulting in asymmetric entrainment from an interaction of their independent entrainment fields (Maynard 2013), resulting in an inward tilting of the flames (Sugawa and Takahashi 1993). Flame tilt between two fires affects fire behavior by increasing the amount of radiant heat transfer to its surface (Byram et al, 1966) and by increasing the horizontal component of convective heat flux towards the flame (Baines 1990). Baldwin et al (1964) theorized that flame tilt is a product of the flow restriction between flames, which causes a pressure drop, which competes with buoyancy. As a fire "sees" an obstacle (such as a wall) this is likely due to the Coanda effect, where the pressure becomes lower due to the limited air supply in the vicinity of the obstacle (Jo et al. 2007). This leads to an imbalance of forces acting on the fire plume, causing it to tilt in the direction of least inflow velocity.

2.2 Experimental Setup and Analysis

The experiment consisted of two 7 in x 7 in x 7 in mesh screen baskets, each filled with 50 grams of aspen wood excelsior fuel. The separation between baskets was varied

and measured between their nearest edges as shown in Figure 2.1. Table 2.1 summarizes the burns done and their respective distances

Figure 2.1 Basket configuration and distance measurement

Table 2.1 Burns in mesh screen baskets (50 grams)

Burn #	**Box Separation (in)**
Burn #1 (Tunnel)	30
Burn #2	30
Burn #3	25
Burn #4	20
Burn #5	15
Burn #6	10
Burn #7	5

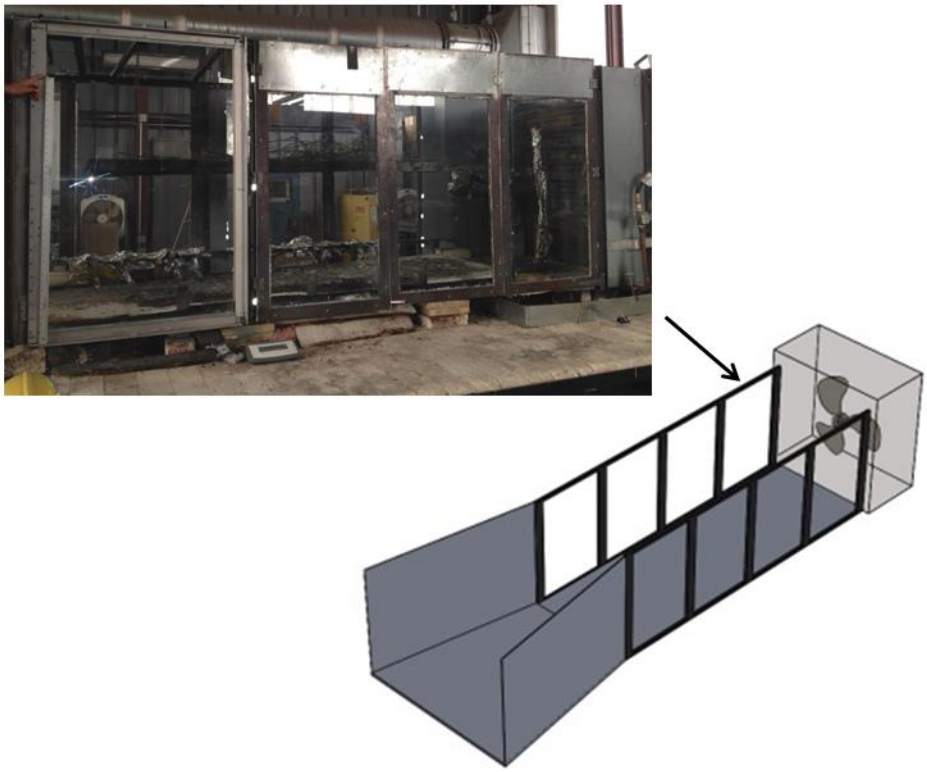

Figure 2.2 Schematic and photo of the Wind Tunnel

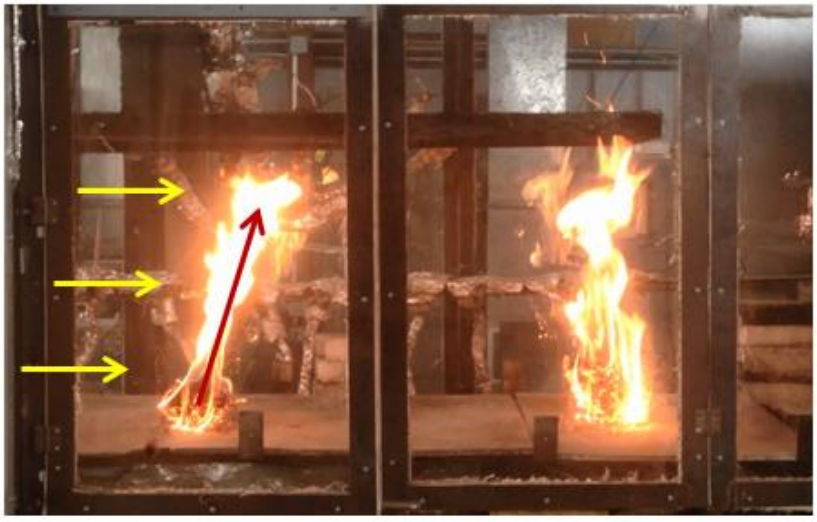

Figure 2.3 Tunnel wall affecting entrainment of fire located at open end. Red arrow shows flame angle and yellow arrows show influence of asymmetric entrainment.

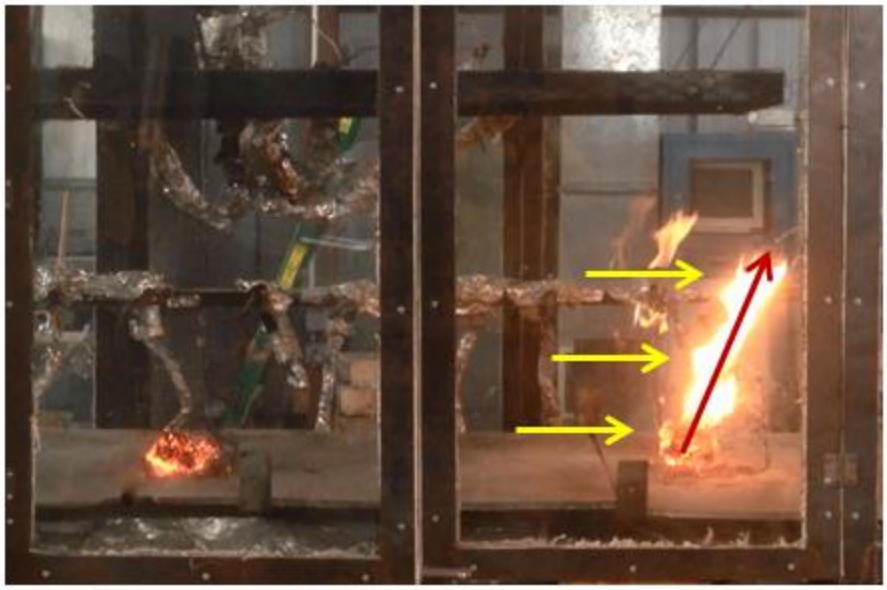

Figure 2.4 Tunnel wall affecting entrainment after fire located at open end was extinguished. Red arrow shows flame angle and yellow arrows show influence of asymmetric entrainment.

The wind tunnel at the USDA Forest Service is designed with the diagram in Figure 2.2. One end of the wind tunnel has a fan while the other end is open. The first burn was done inside the wind tunnel with a 30 inch separation as shown in Figure 2.3. The fan stayed off because wind is not required for this experiment. It was observed that the fire towards the open end always had more flame tilt, while the fire near the fan typically showed no noticeable flame tilt. Once the fire on the open end extinguished, the fire by the fan side started to tilt as shown in Figure 2.4. It was concluded that the scale of this experiment was too large for the scale of the wind tunnel, and that the fire could not obtain symmetrical entrainment. To address this, the next burns were done outside of the wind tunnel.

Burns #2-7, showed no significant flame tilt or fire merging. But for Burns #6 and #7, instead of the fuel burning evenly downwards, it was burning at a slope (Figures

2.5 and 2.6). It is speculated that this could be due to preheating effects by the increased amount of radiant heat transfer from the other basket.

Figure 2.5 Burn #6. Sloped burnt fuel is noticeable. White arrows mark the radiant preheating of the fuel

Figure 2.6 Burn #7. Sloped burnt fuel is noticeable. Red arrows mark the radiant preheating of the fuel

The two fuels were taken out of the boxes and positioned into rectangular configurations to observe if whether the fuel bed configuration was preventing flame tilting and fire merging. The opposite ends of the fuel configurations were ignited so they would burn towards each other and merge. The junction zone is where the two fires join to become one fire. These burns are summarized in Table 2.2 and presented in Figure 2.7

Table 2.2 Burns outside mesh screen baskets

Burn #	Individual Mass (g)	Total Mass (g)	Separation of Fuel (in)
Burn #8	50	100	0
Burn #9	100	200	6
Burn #10	200	400	2 to 3

Figure 2.7 Pictures of burns with rectangular fuel configurations. Red arrows represent tilt angle.

In Burn #8, with the specified configuration, there was some tilting but not very significant. In Burn #9, the flames were bigger and would see each other when a critical distance was reached. In Burn #10, the flames were even bigger and there was obvious tilting/merging. The critical distance between the flames in Burn #10 was more than Burn #9.

After analyzing these burns, it is speculated that fire merging and flame tilting is a function of:

- Amount of fuel
- Size of flame
- Fuel configuration
- Separation distance of flame to another flame / obstacle

These variables are important because of entrainment. The amount of entrained air directly corresponds to the amount of fuel and the size of flame. Fuel in the mesh screen boxes has a cylindrical fuel configuration. Figure 2.8 and Figure 2.9 show the entrainment profiles of the cylindrical and rectangular fuel configurations. Figure 2.10 shows overlapping entrainment profiles when the two flames in the rectangular configuration reach a critical distance, causing them to see each other. In the cylindrical configuration there is less overlapping entrainment in comparison, even at small distances of 5 inches. The distance between flames will influence the amount of overlapping entrainment. The critical distance of flame from an obstacle (i.e. wall) will create asymmetrical entrainment causing flame tilting.

The open burns summarized in Table 2.3 were done with the configurations found in Figure 2.11 to 2.14 to confirm tilting in the asymmetrical and overlapping entrainment cases is a function of amount of fuel, size of flame, fuel configuration, and separation distance.

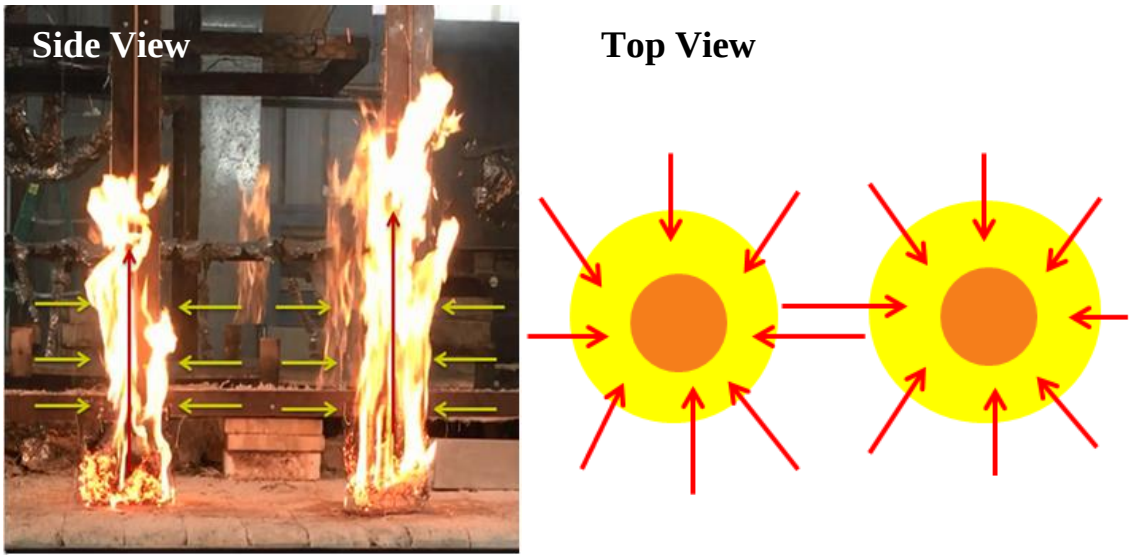

Figure 2.8 Entrainment profile of fire in cylindrical fuel configuration. In the side view, entrainment profile is mapped by yellow arrows and the red arrows give the flame angle. In the top view, fuel is represented in yellow, fire is represented in orange, and the red arrows map entrainment.

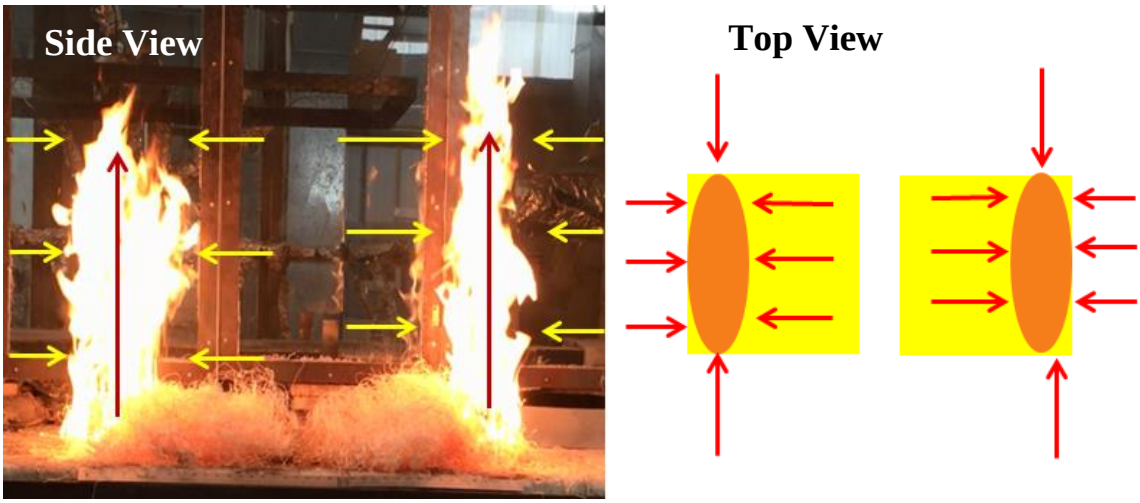

Figure 2.9 Entrainment profile of fire in rectangular configuration. In the side view, entrainment profile is mapped by yellow arrows and the red arrows give the flame angle. In the top view, fuel is represented yellow, fire is represented orange, and the red arrows map entrainment.

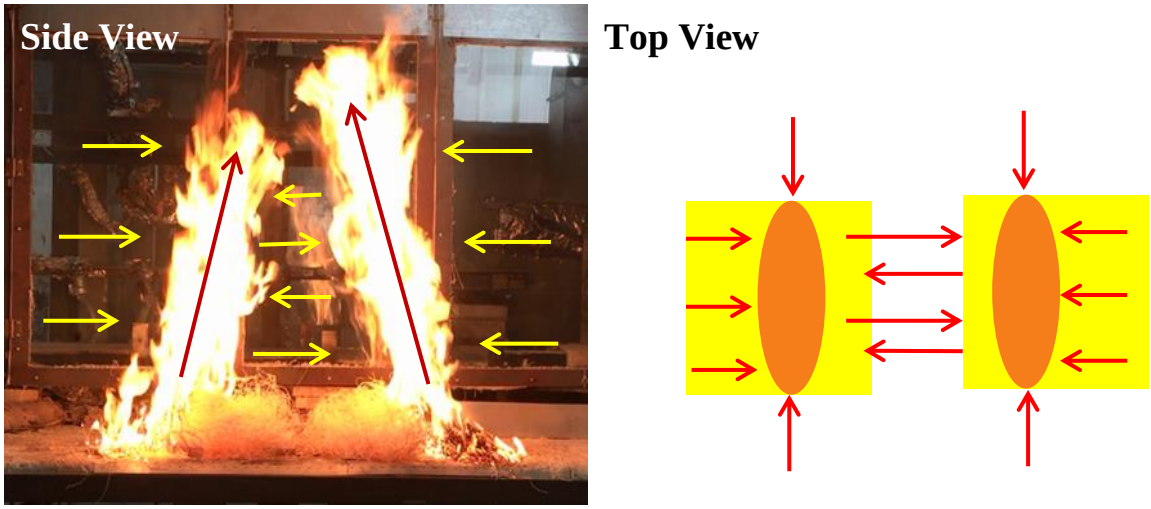

Figure 2.10 Overlapping entrainment profile of fire in rectangular configuration. In the side view, entrainment profile is mapped by yellow arrows and the red arrows give the flame angle. In the top view, fuel is represented in yellow, fire is represented in orange, and the red arrows map entrainment.

Burns #1-2 exhibit the Figure 2.11 configuration, Burns #3-4 exhibit the Figure 2.12 configuration, and Burns #5-6 exhibits the Figure 2.13 and 2.14 configurations respectively.

The fires in Burns #1 and #2 did not significantly see the wall, while Burn #3 and #4 showed the fire would see the wall at a critical distance and touched the wall towards the end of the burn (Figure 2.15). In Figure 2.12, the mapped entrainment profile shows the fire would have a more significant asymmetrical entrainment than Figure 2.11 due to the length of the *Y* dimension. Burn #5 displayed significant tilting at a critical distance. The two fires merged and reached junction zone when flames were at its peak size (Figure 2.16). In Burn #6, the two fires did not significantly see each other. Figure 2.13 shows the fires would have more overlapping entrainment profiles than Figure 2.14 due to comparison of the *Y* dimension.

Table 2.3 Open burns

Burn #	**Mass (g)**	***X* (in)**	***Y* (in)**	**Height (in)**	***d* (in)**
Burn #1	200	31	12	5.5	0
Burn #2	400	31	12	6.5	0
Burn #3	200	12	24	4.5	0
Burn #4	400	12	24	8	0
Burn #5	400	12	24	9	13.25
Burn #6	400	24	12	9	13.25

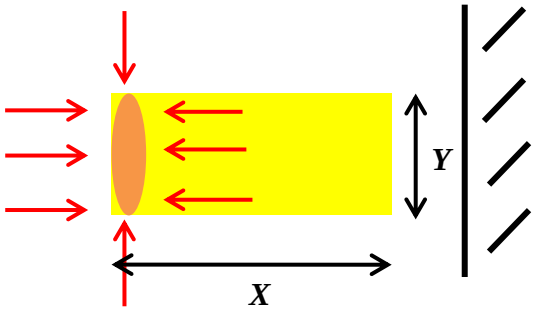

Figure 2.11 Fuel configuration (yellow) for *Y* less than *X*. Orange represents ignition position and red arrows represent entrainment profile.

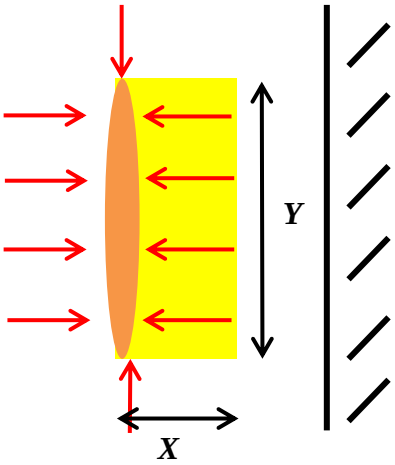

Figure 2.12 Fuel configuration (yellow) for *Y* greater than *X*. Orange represents ignition position and red arrows represent entrainment profile.

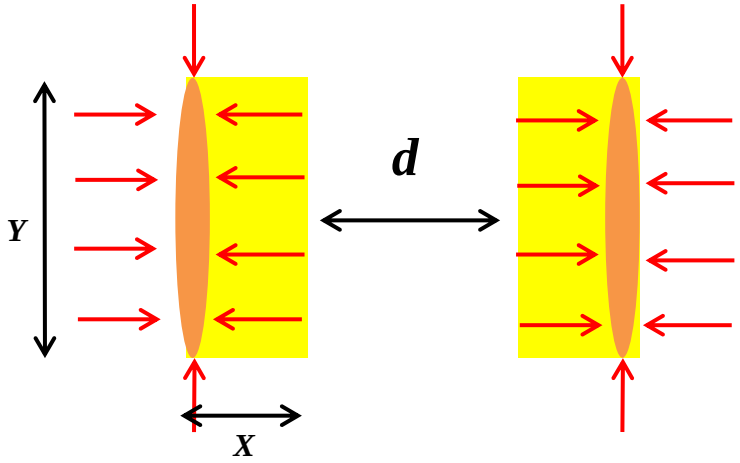

Figure 2.13 Fuel configuration (yellow) for *Y* greater than *X* separated by a distance *d*. Orange represents ignition position and red arrows represent entrainment profile.

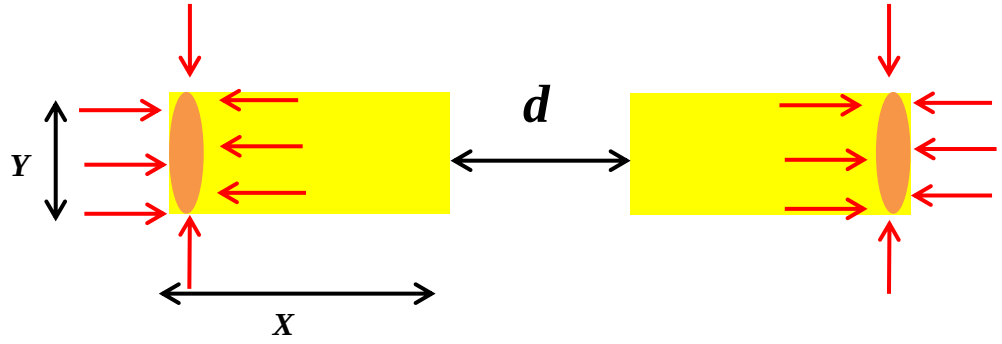

Figure 2.14 Fuel configuration (yellow) for *Y* less than *X* separated by a distance *d*. Orange represents ignition position and red arrows represent entrainment profile

Figure 2.15 Burn #3 and #4 with Figure 2.12 configuration exhibiting flame tilting at a critical distance (left) and fire touching wall towards the end of burn(right).

Figure 2.16 Burn #5 with Figure 2.13 configuration exhibiting flames seeing each other at a critical distance (left) and merging, creating junction zone (right).

2.3 Conclusion

It is concluded from the experiments done outside of wind tunnel that fuel configuration has significant influence in fire merging due to asymmetric and overlapping areas of entrainment. We speculate that the difference of 200 grams of fuel was not significant enough to influence tilting in Burns #1 and #2. If the difference in amount of fuel was greater, the fire might see the wall due to increased entrainment. The critical distance for Burn #4 might be greater than Burn #3, but it was not visually apparent. Image processing needs to be done in order to correctly determine the critical distance. Although we did not vary distance between fuels of the configurations found in Figure 2.13 and 2.14, it is apparent that had *d* been greater for Burn #5, merging would not be seen due to the fire being able to have fully symmetrical entrainment.

2.4 References

Albini, Frank A. 1981. "A Model for the Wind-Blown Flame from a Line Fire." Combustion and Flame 43 (C): 155–74. doi:10.1016/0010-2180(81)90014-6.

Baines, Peter G. 1990. "Physical Mechanisms for the Propagation of Surface Fires." Mathematical and Computer Modelling 13 (12): 83–94. doi:10.1016/0895-7177(90)90102-S.

Baldwin R, Thomas PH, Wraight HGG (1964) The merging of flames from separate fuel beds. Fire Research Note 551. Boreham Wood Fire Research Station. (Boreham Wood, Hertfordshire)

Byram GM, Clements HB, Bishop ME, and Nelson Jr. RM (1966) Final report - Project Fire Model: an exploratory study of model fires. USDA Forest Service, Southeastern Forest Experiment Station, Office of Civil Defense Contract OCD-PS-65-40. (Asheville, NC).

Finney, Mark A., Jack D. Cohen, Sara S. McAllister, and W. Matt Jolly. 2013. "On the Need for a Theory of Wildland Fire Spread." International Journal of Wildland Fire 22 (1): 25–36. doi:10.1071/WF11117.

Jo, Akihide, Tomoaki Nakao, Akito Yanagisawa, Kaoru Wakatsuki, and Yoshifumi Ohmiya. 2007. "Fire Plume Ejected from an Opening in Unconfined Space Part 3 Behavior of Fire Plume Ejected from an Opening in the Vicinity of Opposed Walls" 26 (4): 511–16.

Maynard, Trevor. 2013. "Fire Interactions and Pulsation – Theoretical and Physical Modeling." University of California, Riverside.

Nelson, Ralph M., Bret W. Butler, and David R. Weise. 2012. "Entrainment Regimes and Flame Characteristics of Wildland Fires." International Journal of Wildland Fire 21 (2): 127–40. doi:10.1071/WF10034.

Pera L, Gebhart B (1975) Laminar plume interactions. Journal of Fluid Mechanics 68, 259-271.

Sugawa, Osami, and Wataru Takahashi. 1993. "Flame Height Behavior from Multi-Fire Sources" 17 (January): 111–17. doi:10.1002/fam.810170303.

Sugawa O, Satoh, H, Oka, Y (1991) Flame height from rectangular fire sources considering mixing factor. Fire Safety Science – Proceedings of the Third International Symposium, 435-444

Weise, David R., and Gregory S. Biging. 1986. “Effects of Wind Velocity and Slope on Fire Behavior,” no. 1981: 1041–51. doi:10.1139/x26-210.

3. Examination of Testicular Thermoregulation

3.1 Introduction

While the previous work focuses on experimentally investigating flame interaction in different fuel configurations to provide more fundamental knowledge of fire. This work focuses on numerically simulating external temperature applications to the testicle in order to provide a stronger fundamental knowledge of biological heat transfer.

The testicles are biologically positioned to externally suspend from the body because sperm develops best few degrees lower than the normal body temperature. The scrotum, testes, and testicular vasculature all have roles in testicular temperature maintenance. The scrotum has a positive temperature gradient (warmer at top than bottom) while the testis has a negative temperature gradient (warmer at the bottom) (Kastelic et al. 1996). These opposing gradients result in a relatively uniform temperature that is lower than that of the body core temperature. This may be due to the arrangement of the vasculature, where testicular artery courses the length of the testis and diverges into smaller arteries, which spread across the surface of the testis. The negative temperature gradient of the testes can be attributed to blood within the branched artery losing heat presumably through dissipation from the scrotum (Kastelic, Coulter, and Cook 1995).

The testicles regulate temperature by heat loss through the scrotal skin and the counter current heat exchange in the pampiniform plexus (Figure 3.1 and 3.2) between

the entering heated arterial blood and returning cooled venous blood. As shown in Figure 3.1 and Equation 3.1, the arterial blood is cooled by the venous blood while the venous blood is warmed by the arterial blood, resulting in them reaching the same temperature, giving the equation that utilizes the basic law of cooling (Sealfon and Zorgniotto 2015).

$$q = W_a C_{pa}(T_{a1} - T_{a2}) = W_v C_{pv}(T_{v2} - T_{v1}) \quad 3.1$$

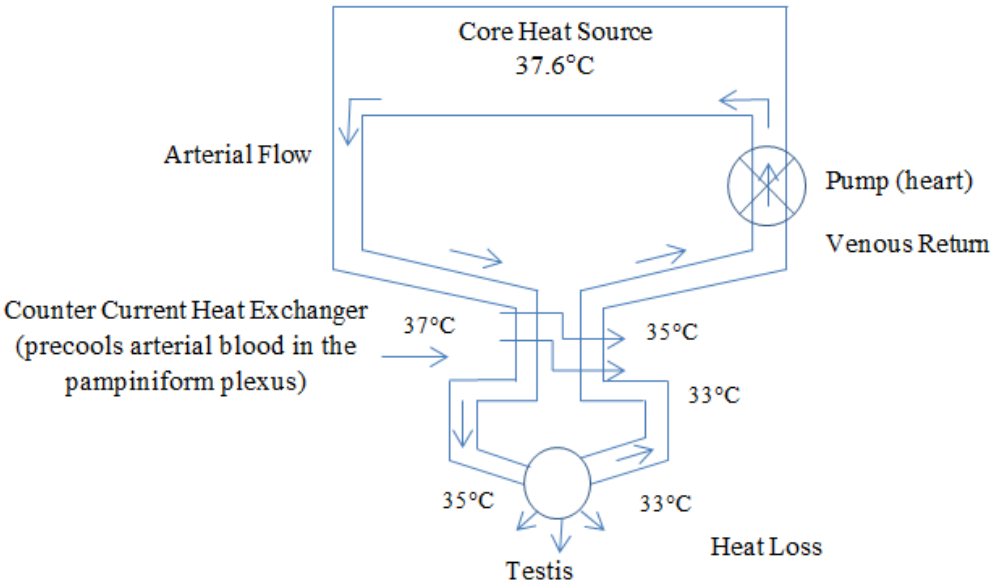

Figure 3.1 Schematic of Scrotum as a fixed heat dissipator, adopted from Sealfon and Zorgniotto 2015

Where q is the heat flow rate, C_{pa} and C_{pv} are the specific heat of arterial and venous blood respectively, W_a and W_v are the mass flow rate of arterial and venous blood, respectively, and T_{a1} and T_{v1} are the initial arterial and venous blood temperatures, respectively. T_{a2} and T_{v2} are equal, as they represent the final arterial and venous temperatures after the counter current heat exchange.

Experiments were conducted by Kastelic in 1996, where the scrotal neck of bulls was insulated in order to understand its effect on semen quality. In one experiment, after insulating the scrotal neck in five bulls for eight days, the semen quality showed lower percentages of normal spermatozoa and higher percentages of spermatozoa with head defects (Kastelic et al. 1996). It was found that the effects can be seen within five days, and that semen quality, after a rise of testicular temperature, is related to the severity of the thermal insulation. It is hypothesized that the heat exchange is sufficient when the scrotum is exposed to cooler temperatures, because core temperature is maintained, while the venous return is much cooler. The testicle thermoregulates by contracting and pulling the testes up against the body and the scrotum limits heat dissipation. The skin increases rugosity to limit surface area exposure (Mariotti et al. 2011). However, when the scrotum is heated, it is unable to dissipate the additional heat and the venous blood temperature rises as a result. Sealfon and Zorgniotto saw that subfertile semen is the result of failure in the heat exchange mechanism (Sealfon and Zorgniotto 2015). There has been great interest in the investigation of testicular thermoregulation failure, as it gives rise of the possibility of male contraceptive solutions.

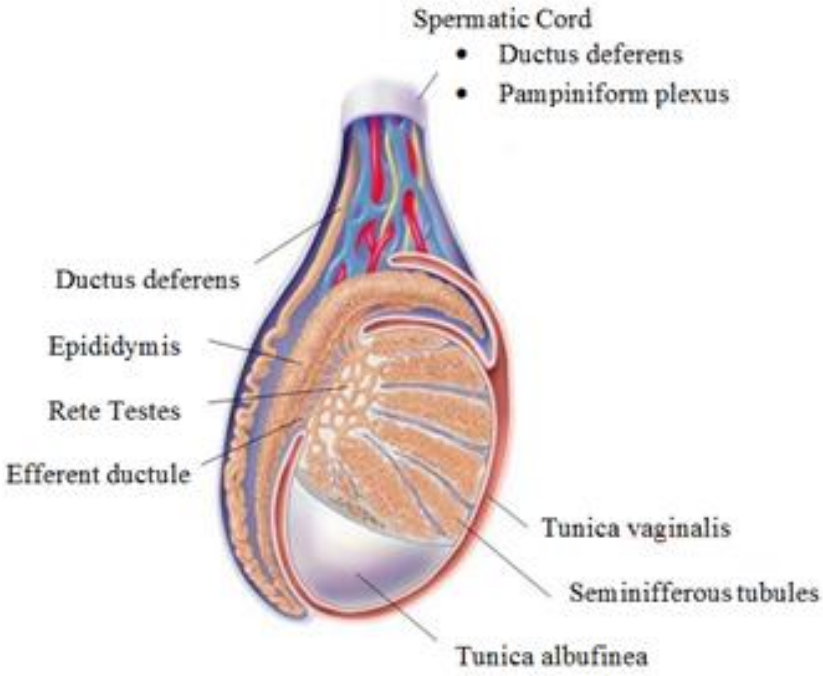

Figure 3.2 Anatomy of testicle (StudyBlue n.d.)

In the Setchell 1998 paper, he investigated how external temperature applications to the scrotum influence spermatogenesis and the amount of time it takes to recover. He examined spermatozoa in rete testis fluid (Figure 3.2) collected from heated testes of rats and rams. The rete testis transport sperm from the seminiferous tubules to the efferent ducts for ejaculation (Figure 3.2) (University of Leeds n.d.). It is in the rete testis that the sperm becomes concentrated. If this does not happen, the sperm that enter the epididymis (Figure 3.2) could be infertile. In rats, the concentration of spermatozoa began to decrease about 1000-fold within 10 days after exposing the testes to 41°C for 60 to 90 minutes. The concentration returned to normal after 38 days. In rams, spermatozoa decreased within 20 days after heating the testes to 40°C for 3 hours, and the

concentration returned back to normal after approximately 38 days, same as the rat (Setchell 1998).

The motivation of this project is to understand sperm cell temperature exposure to further fundamental knowledge of biological heat transfer in order to advance towards a possible male contraceptive. Penne's bioheat transfer equation has been used to describe the effects of countercurrent heat exchange and capillary bleed off on local tissue heat transfer (Weinbaum and Jiji 1985). For this project, it is specifically used to investigate how cell metabolism and perfusion of tissue influence thermoregulation. The Finite Element Method was performed using COMSOL Multiphysics. This simulation software has been historically used for medical research purposes because of its convenient heat transfer subsection that utilizes the bioheat equation. Gonzalez, for example, used COMSOL for thermal simulation of breast tumor (González 2007).

The analysis of testicular thermal application is performed through two stages. The primary stage is to determine the transient heat transfer solution for one heated testicle. After this is achieved, the secondary stage is to model two heated testes side by side to understand how they influence each other. Penne's bioheat equation is as follows:

$$\rho C \frac{\partial T}{\partial t} - k \nabla^2 T = h_m + h_b \qquad 3.2$$

where h_m represents metabolic heat generation and the perfusion term, h_b, (Equation 3.3), represents the rate of heat transfer per unit volume of tissue. This perfusion term utilizes the cooling equation (Equation 3.1), and is expressed as:

$$h_b = \nu\rho_b C_b(1-\kappa)(T_a - T) \qquad 3.3$$

Typical values of the terms in the bioheat equation are given in Table 3.1:

Table 3.1 Terms and values of the Penne's bioheat equation (González 2007, Wissler 2012)

Density of tissue	ρ	$1060\,\frac{kg}{m^3}$
Heat capacitance of tissue	C	$3600\,\frac{J}{kg \cdot K}$
Specific heat of tissue	k	$0.5\,\frac{W}{m \cdot K}$
Metabolic heat generation	h_m	$450\,\frac{W}{m^3}$
Perfusion rate per unit volume of tissue	ν	$0.0052\,\frac{1}{s}$
Density of blood	ρ_b	$1025\,\frac{kg}{m^3}$
Specific heat of blood	C_b	$3617\,\frac{J}{kg \cdot K}$
Factor for incomplete thermal equilibrium between blood and tissue	κ	$0 \geq \kappa \leq 1$ $for\ this\ project$ $\kappa = 0.5$
Arterial blood temperature	T_a	$36.8\ °C,$ $310.15\ K$

3.2 Isolated Testicle Data

For simplicity, the analysis begins by solving the diffusion equation, where the metabolic and perfusion terms are set to zero, (Equation 3.4) for the transient heating of a sphere:

$$\rho C \frac{\partial T}{\partial t} - k \nabla^2 T = 0 \qquad 3.4$$

The solution to the above equation is referred to in this text as base temperature, T_B. The procedure consists of the following steps in COMSOL and is illustrated in Figure 3.3:

- Form a circle that is 2 cm in radius (testicle is roughly 25 cubic centimeter in volume) and is axis symmetric in spherical coordinates at R = 0
- Apply the initial condition of 305.15 K throughout the circle (average temperature of a testicle).
- Apply the boundary condition of external temperature 315.15 K at R = 2 cm.
- Create mesh

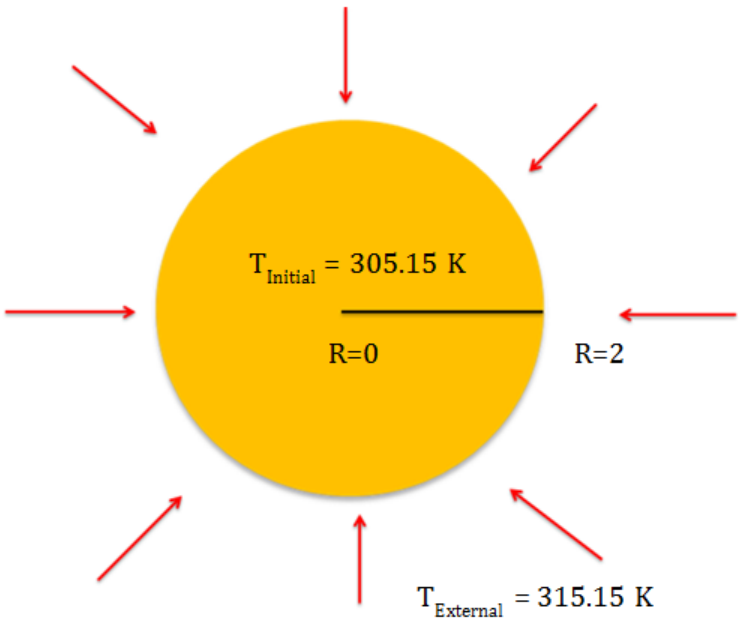

Figure 3.3 Visualization of COMSOL analysis for isolated testicle

Figure 3.4 shows the temperature profile from R = 0 cm to R = 2 cm of the isolated testicle being heated for 30 minutes. Each line of the plot represents a 2 minute increment.

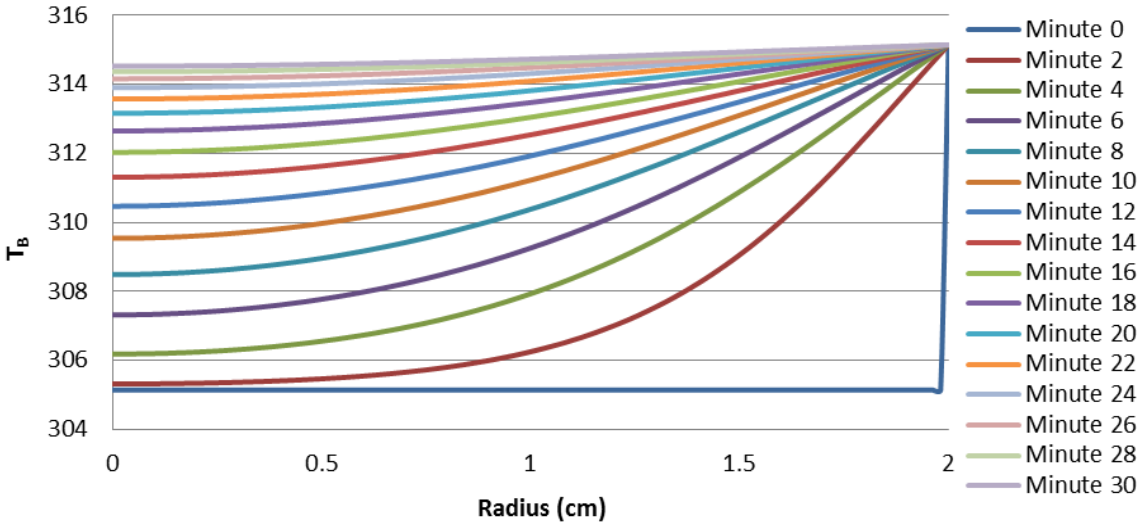

Figure 3.4 Development of the base temperature equation (Equation 3.4)

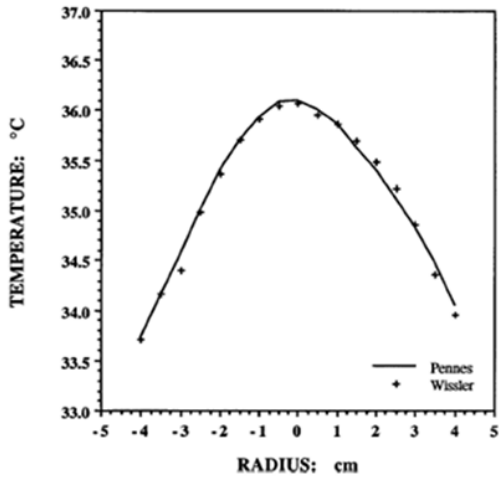

Figure 3.5 Penne's Bioheat equation graph for heating of arm (Wissler 2012)

Next, the metabolic and perfusion terms are applied. According to Wissler, the analytical plot of Penne's heat transfer equation should look parabolic if the external

temperature of an arm is lower than the core (Wissler 2012) (Figure 3.5). Knowing this, we should expect our solution to be reversed parabolic, as the external temperature is higher than the core temperature of the testicle.

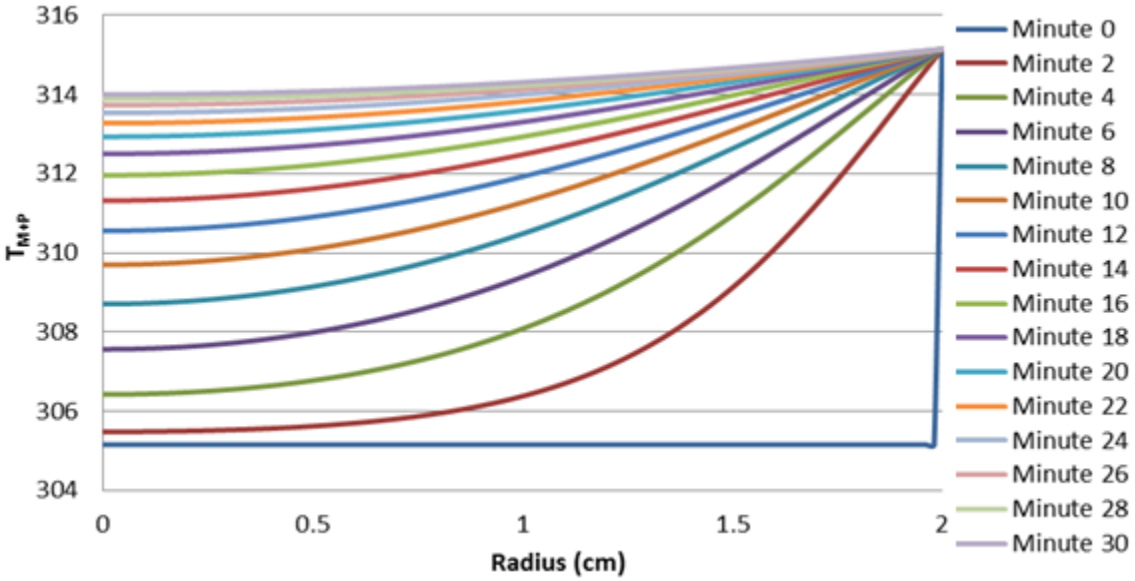

Figure 3.6 T_{M+P} vs. Radius (cm)

Figure 3.6 uses the bioheat equation (Equation 3.2) to obtain the temperature field development of an isolated testicle. It plots temperature as a function of radius, using the same boundary conditions and time range as before. The solution is labeled $T_{M+P,}$ to express the solution's implementation of the metabolic and perfusion terms. It is normalized by T_B, presented in Figure 3.7, to investigate the influence of metabolic and perfusion terms.

Next, the influence of perfusion and metabolic terms are investigated separately. T_M and T_P are solutions of the bioheat equation when the perfusion and metabolism are set to zero, respectively. It is observed that the plot line of minute 30 for Figure 3.8 is

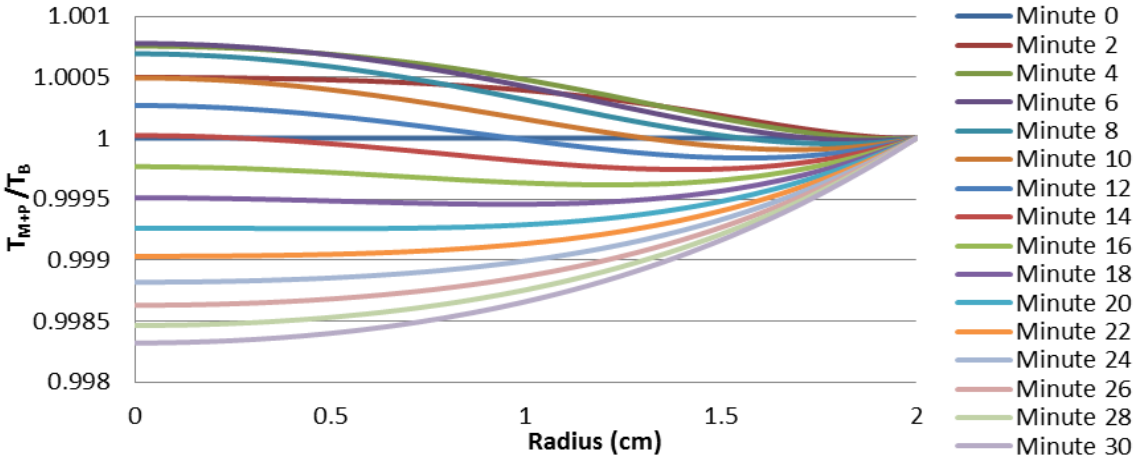

Figure 3.7 Influence of metabolism and perfusion

lower compared to Figure 3.7 suggesting that the metabolic term raises temperature, which is shown in Figure 3.9.

It is seen from Figure 3.7 and 3.8 that the perfusion term initially helps raise the temperature of the testicle. But when the temperature of the testicle is above the temperature of blood (310.15 K), the blood instead cools the testicle. This is apparent in Figure 3.7 and Figure 3.8, where we can see that the normalized temperature at steady

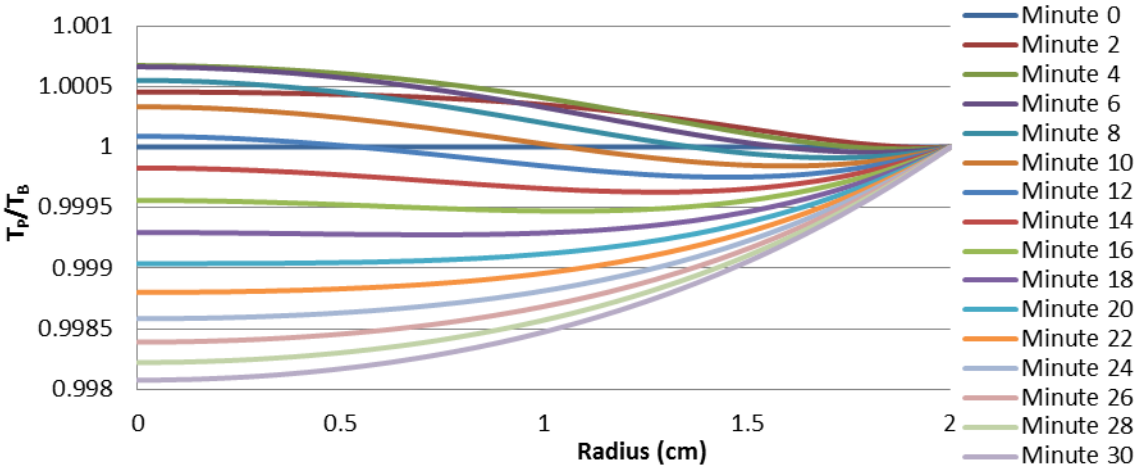

Figure 3.8 Influence of perfusion term

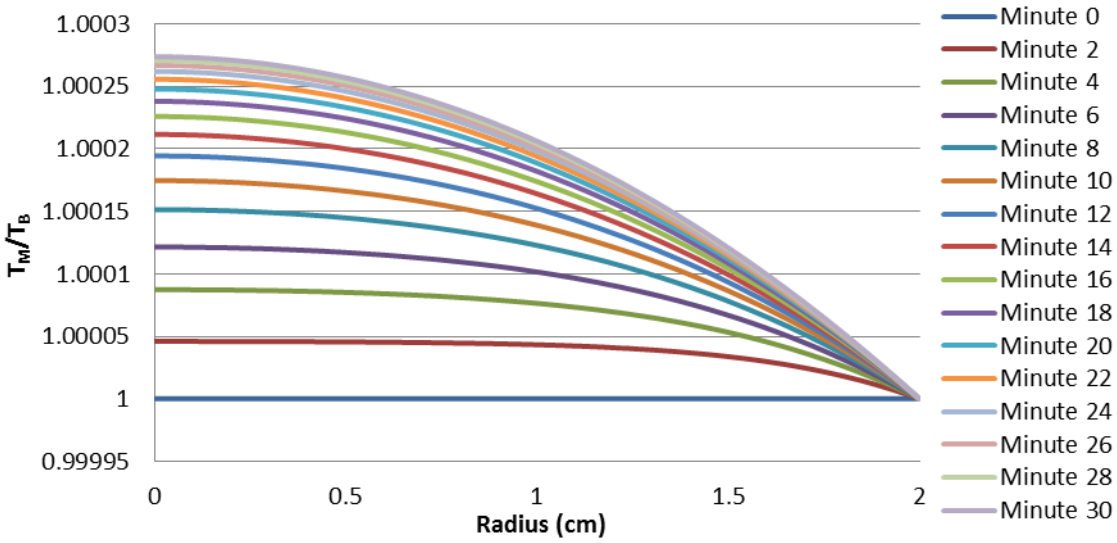

Figure 3.9 Influence of metabolism term

state is below unity. The metabolic term is shown to only raise the temperature of the testicle. However, the conclusion is metabolic and perfusion terms of Penne's bioheat equation do not have a significant effect on the thermoregulation processes of the testicle. These effects are on the order of one hundredths of percent.

After obtaining this data, the following plots show the instantaneous temperature (blue), the running average temperature at one-minute intervals (red), and the average temperature over the last five minutes (green). This was done on testicle cells at positions R = 0 cm (center), R = 0.5 cm, and R = 0.76 cm in Figure 3.10, Figure 3.11, and Figure 3.12 respectively.

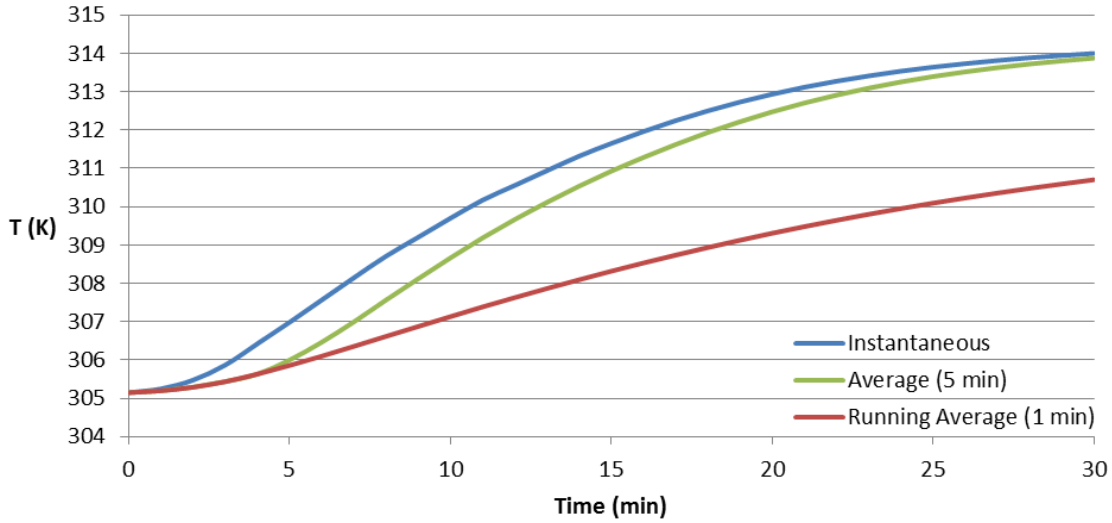

Figure 3.10 Temperature Average Plot at the center (R = 0 cm)

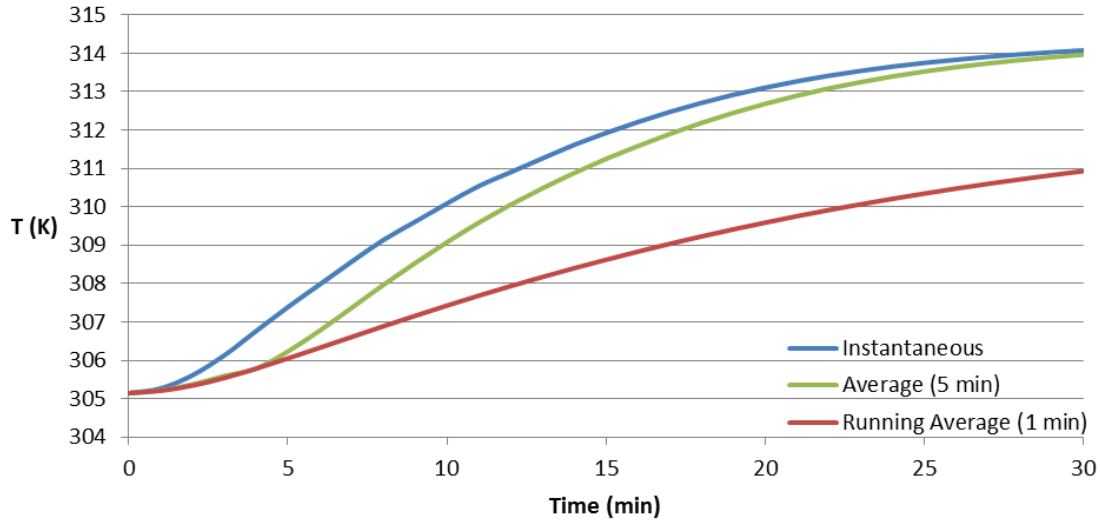

Figure 3.11 Temperature Average Plot at R = 0.5 cm

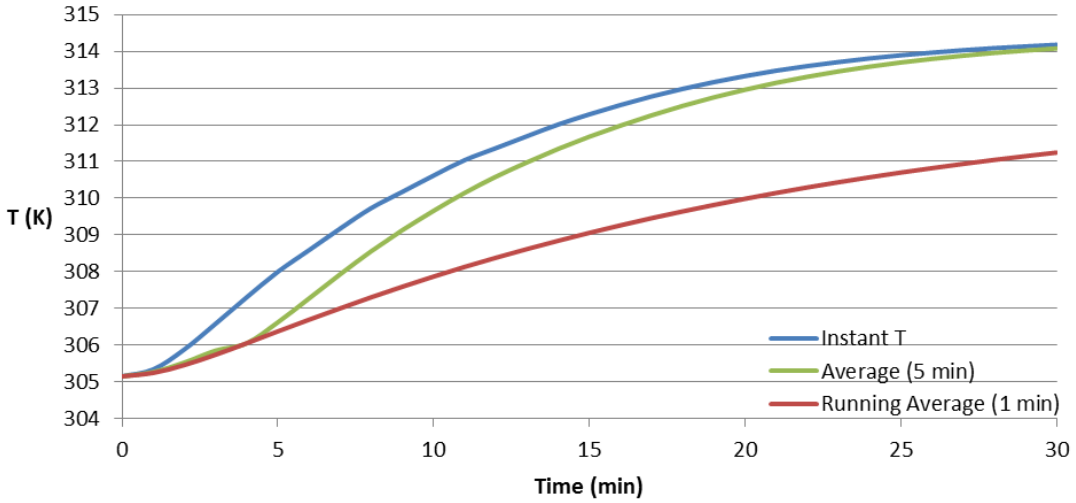

Figure 3.12 Temperature Average Plot at R = 0.76 cm

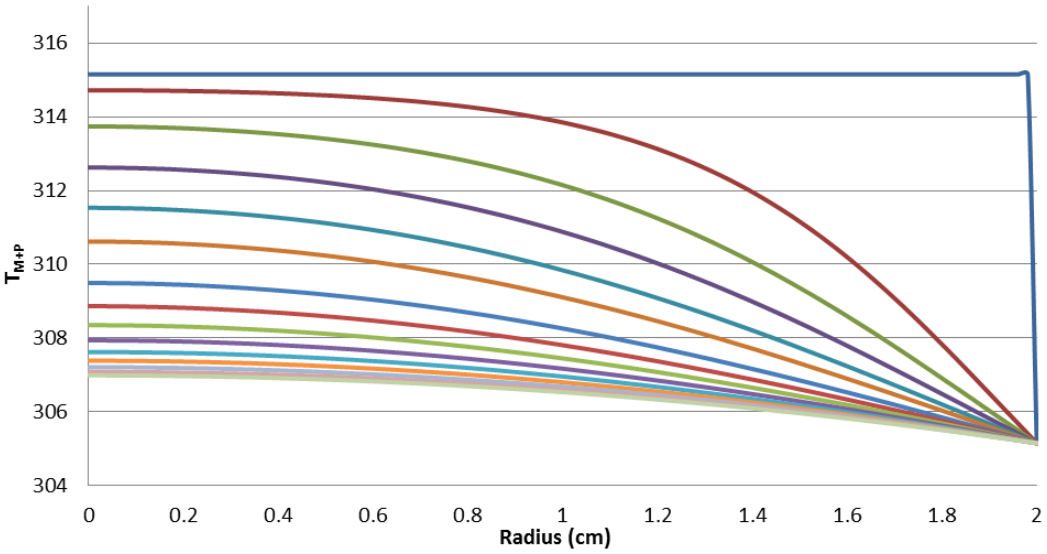

Figure 3.13 Cool Down Plot

Figure 3.13 shows how the testicle, at 315.15 K, would cool once the external heat source is removed. The plot is essentially an inverted plot of the testicle being heated.

3.3 Non-isolated Testicle Data

After completing the primary stage of obtaining the temperature profile of one testis, the secondary stage was to determine the temperature profile of two testes side by side utilizing the Penne's bioheat transfer equation. The goal of this was to understand how the two testes influence each other with an applied external heat.

In a simple heat transfer problem, when a uniform external temperature is applied symmetrically to a one-dimensional box, the heat flux at the center is equal to zero. As diagramed in Figure 3.14:

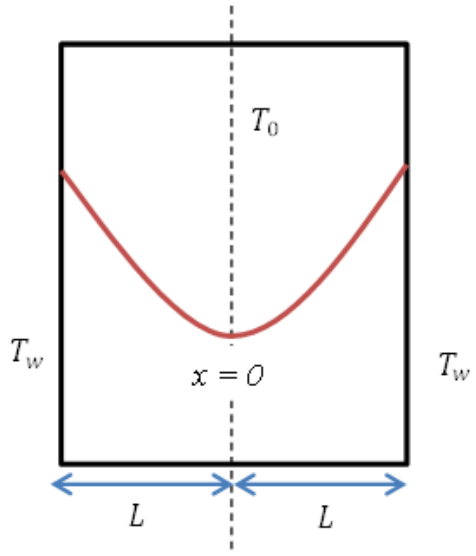

Figure 3.14 Symmetric heat transfer schematic of box. Red parabolic line represents the temperature distribution

We specify the boundary condition on both sides of the wall as

$$T = T_w \; at \; x = \pm L$$

where T_w is the temperature at the walls, and T_0 is the initial temperature of the box. The general solution is

$$T = C_1 \frac{x^2}{2} + C_2$$

Solving this, we can see the temperature and heat flux at the center and at the wall are

$$@x = 0;\ T_0 = C_2;\ \frac{\partial T}{\partial x} = 0$$

$$@x = L;\ T_w = C_1 \frac{L^2}{2} + C_2;\ \frac{\partial T}{\partial x} = C_1 L$$

From this example, we can see that when two spheres are placed next to each other with an external heat source applied symmetrically to its perimeter; the heat flux at the center is equal to zero (Figure 2.15).

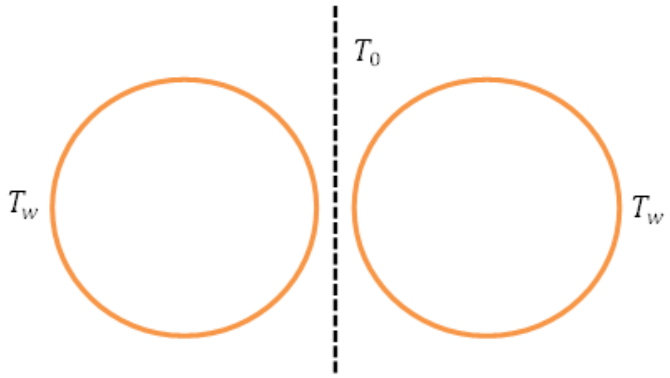

Figure 3.15 Symmetric heat transfer schematic of testicle with zero heat flux at center

The solution procedure consists of the following steps to model the left testicle in COMSOL Multiphysics and is illustrated in Figure 3.16:

- Create a circle that is 2 cm in radius (testicle is roughly 25 cubic centimeter)

- Apply an initial condition of 305.15 K (average temperature of a testicle) to the entire circle.
- Apply a boundary condition of 315.15 K to ¾ of the circle's perimeter
- Apply a boundary condition of $\partial T/\partial x = 0$ to the remaining ¼ of the circle's perimeter
- Create mesh

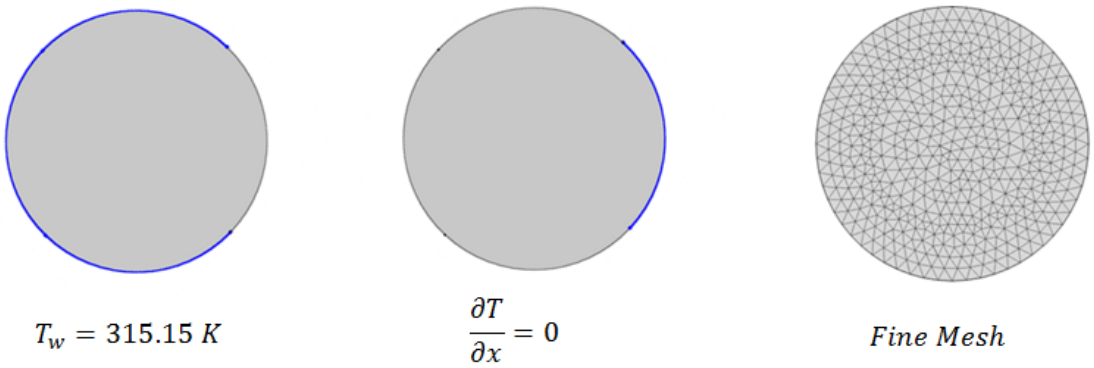

Figure 3.16 Comsol analysis of non-isolated testicle

The same time range of 0 to 30 minutes in increments of 2 minutes was applied. At minute 0 (Figure 3.17), the circle is predominantly blue because the external temperature is primarily present at T_w and has not yet spread. At minute 16 (Figure 3.18) and 30 (Figure 3.19)there is a temperature distribution with the lighter color located in the area of no heat flux. Theoretically, the temperature profile with the heated testes side by side is shown in Figure 3.19:

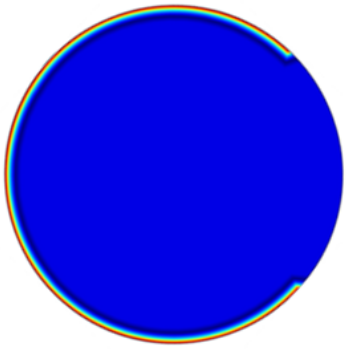

Figure 3.17 Initial temperature distribution with blue and red regions coresponding to 305.15 K and 315.15 K, respectively.

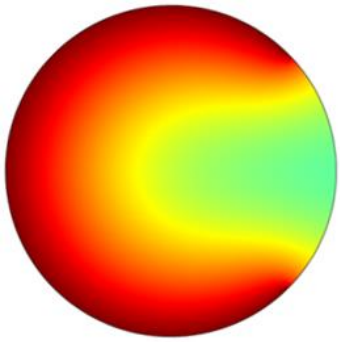

Figure 3.18 Temperature Profile at Minute 16. For color scale, refer to Figure 3.19

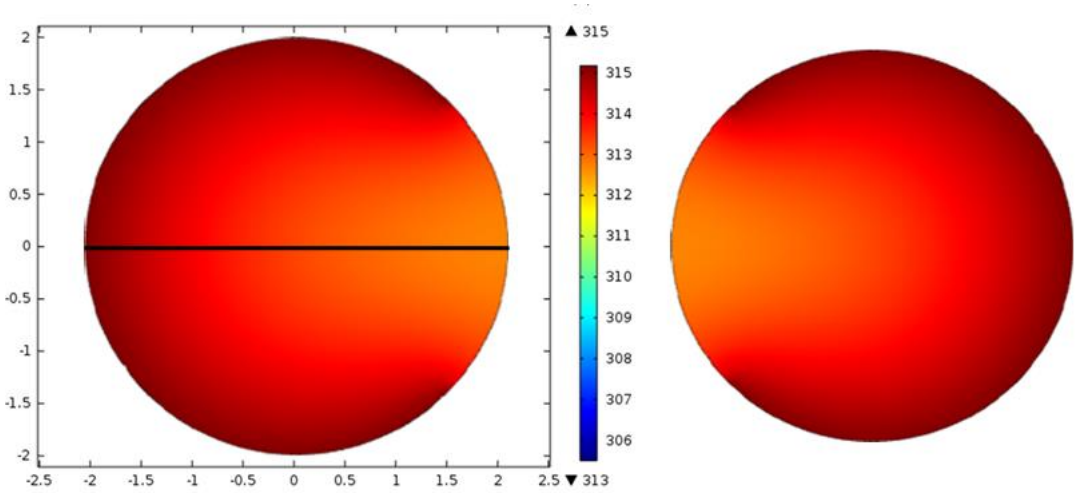

Figure 3.19 Final temperature distribution with two testicles side by side with color scale and cut line for data export

A cut line was applied horizontally though the center of the left testicle, as shown in Figure 3.19 and the data was exported to obtain a plot of the temperature distribution. The same data analysis plots as previous were made to investigate how the metabolic and perfusion terms influence the heating of the testicle.

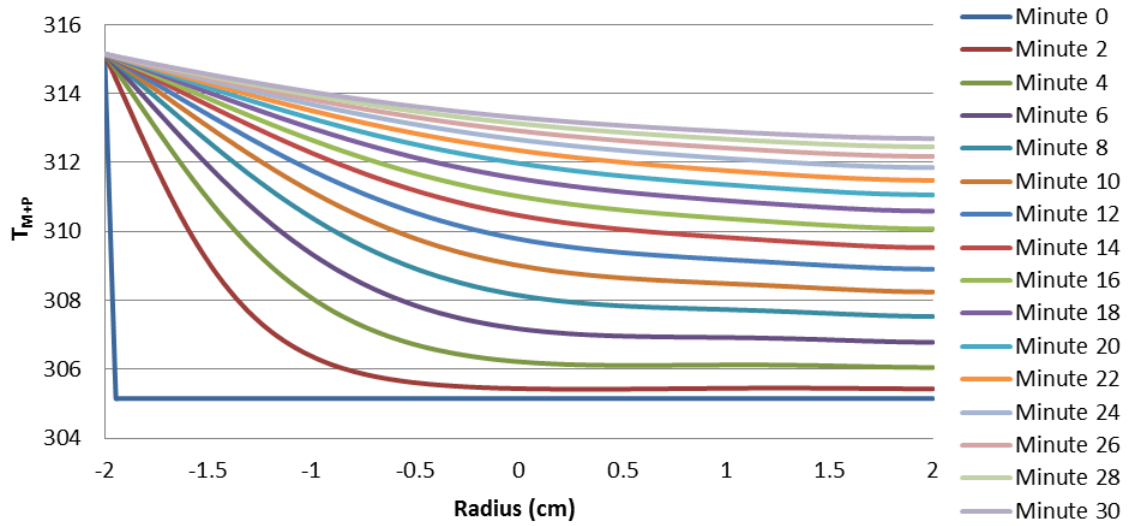

Figure 3.20 T_{M+P} vs. Radius (cm)

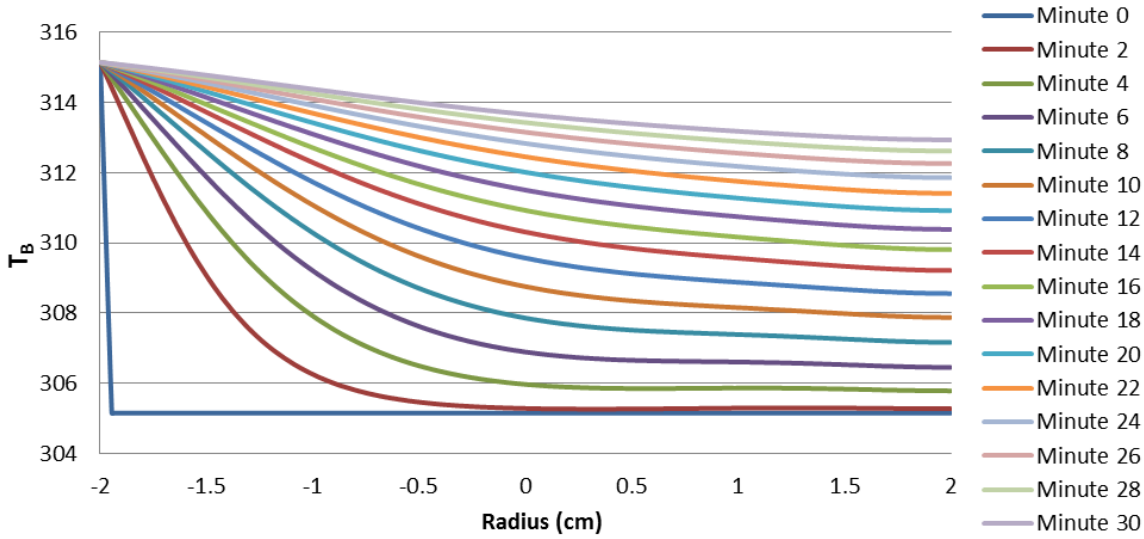

Figure 3.21 Development of the base temperature equation

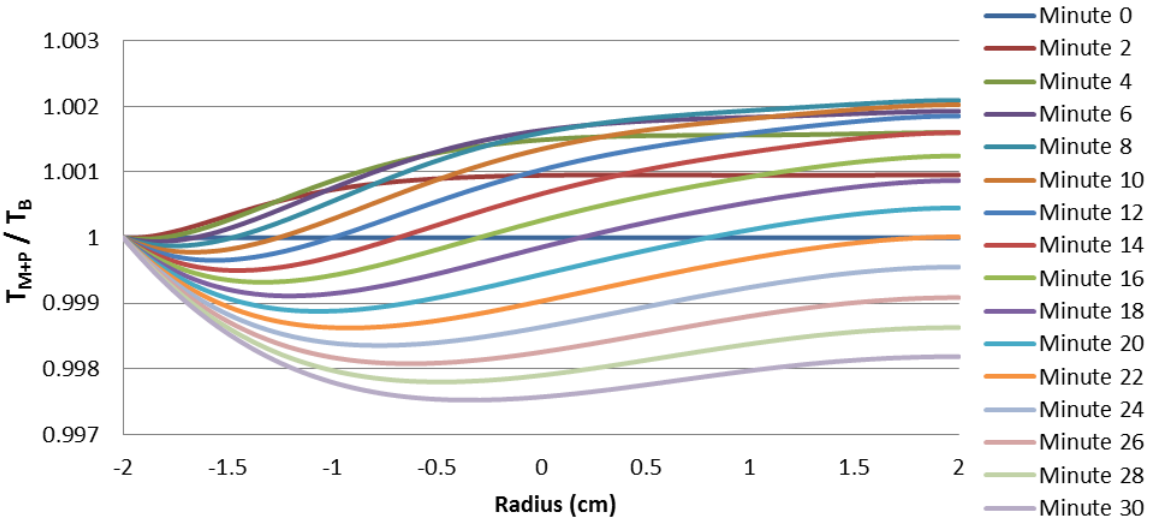

Figure 3.22 Influence of metabolism and perfusion

When comparing the two plots of Figure 3.20 and Figure 3.21, we can see the influence of the extra terms in T_{M+P} is apparent. Figure 3.22 shows that the metabolic and perfusion term influences the bioheat equation, but only within very few decimal places. Figure 3.23 and Figure 3.24 show the investigation of the perfusion and metabolic terms separately

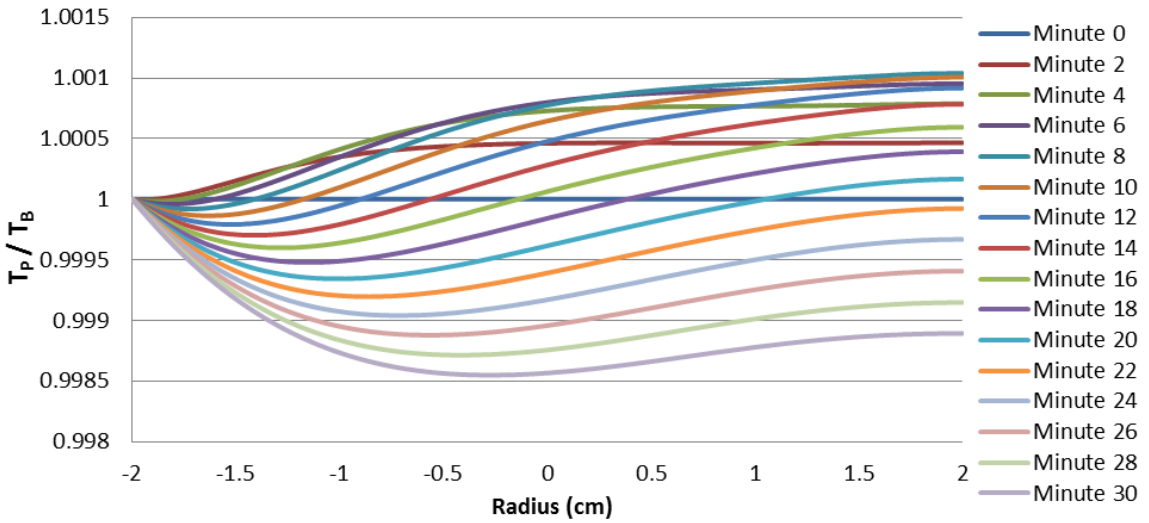

Figure 3.23 Investigation of perfusion term

From the T_{M+P}/T_B plots and the T_P/T_B plots, we can see that the arterial blood initially helps raise the temperature of the testicle from 305.15 K while it is heating up from the external temperature source, but as the overall temperature of the testicle exceeds the blood temperature, the blood begins to cools the testicle rather than heat it. This explains the behavior found in Figure 3.22 and Figure 3.23 where the normalized temperature initially descends and later rises. As expected, the metabolic term of the bioheat equation only raises the temperature of the testicle.

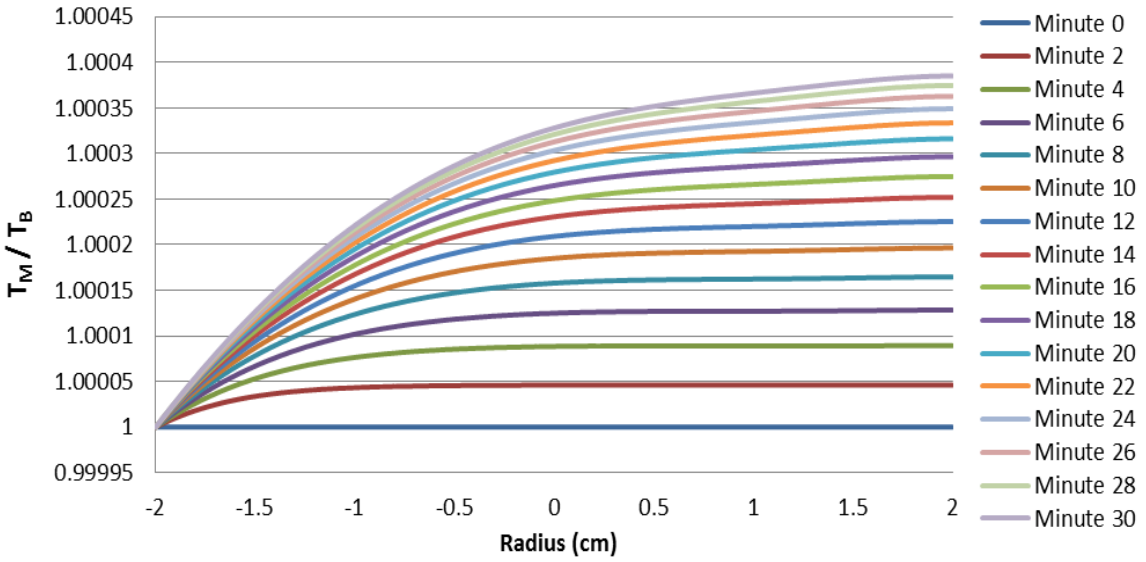

Figure 3.24 Investigation of metabolism term

After obtaining this data, the following plots were made to show the instantaneous temperature (blue), the running average temperatures at one-minute intervals (red), and the average temperature over the last five minutes (green). This was done on testicle cells at radial positions R = 0 cm (center), R = 0.5 cm, and R = 0.76 cm (Figure 3.25, Figure 3.26, and Figure 3.27, respectively).

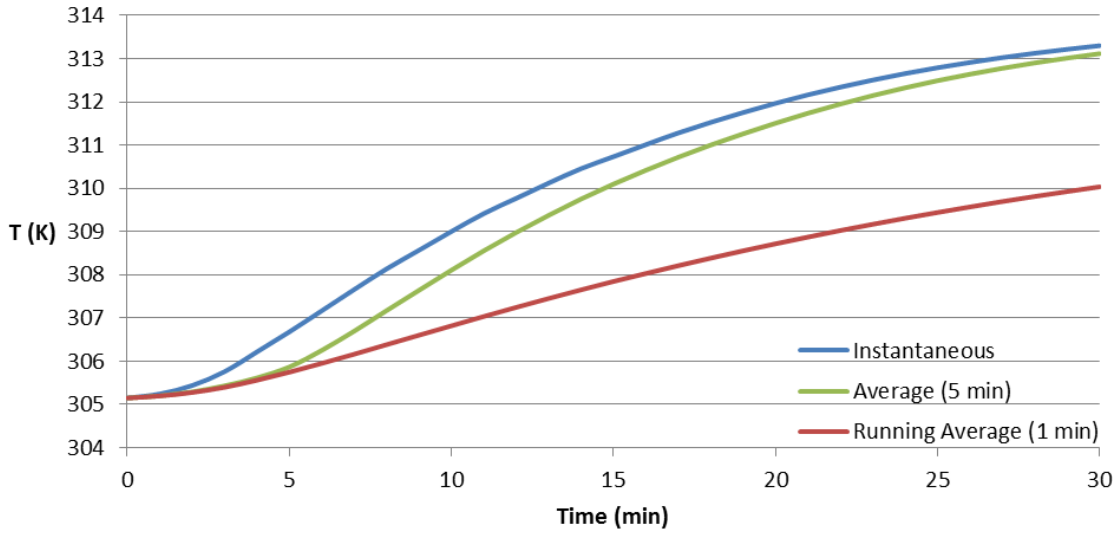

Figure 3.25 Temperature Average Plot at R = 0 cm

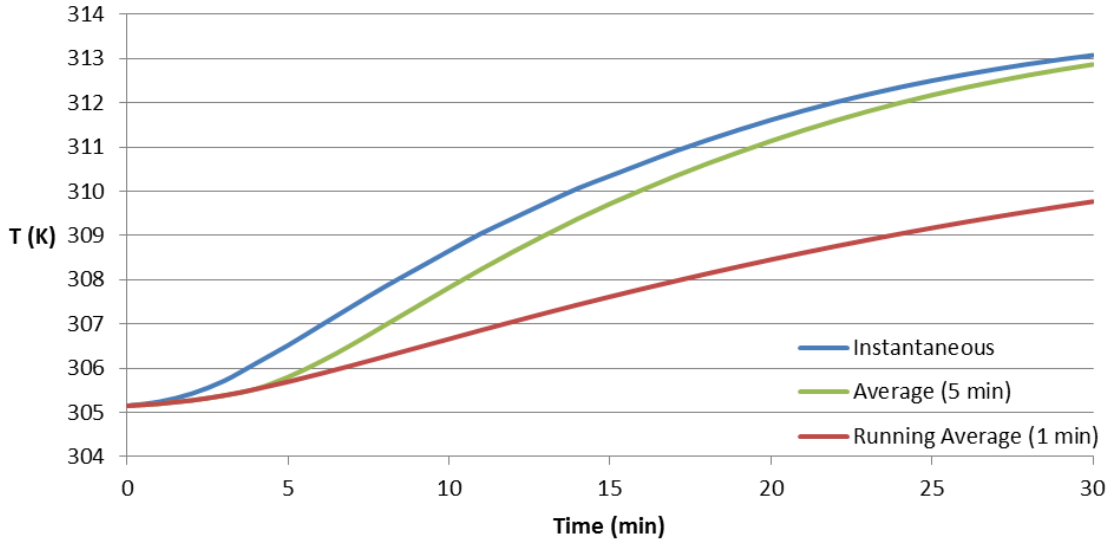

Figure 3.26 Temperature Average Plot at R = 0.5 cm

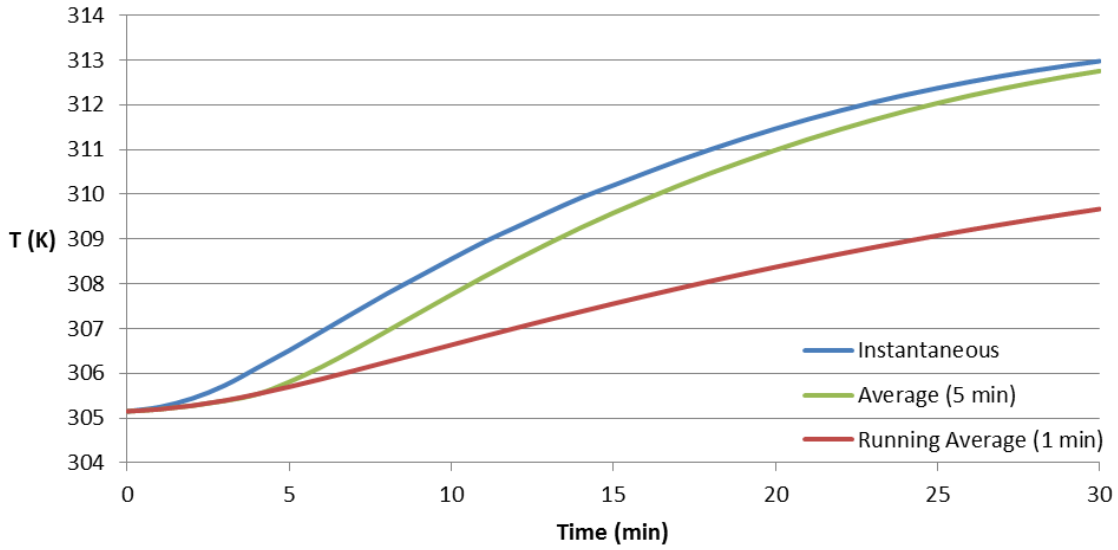

Figure 3.27 Temperature Average Plot at R = 0.76 cm

3.4 Conclusion

In the isolated and non-isolated testicle model, it was shown that the metabolism and perfusion terms did not significantly influence the heating of the testicle. Figures 3.28 and 3.29 plot the non-dimensional temperature distribution of the heated testicle. It can be seen that the testicle approached steady state after roughly 15 minutes.

Table 3.2 gives the average temperature for the cells at the specified radius on minute 15. The isolated and non-isolated temperature values at position R= (center) 0 cm, 0.5 cm, and 0.76 cm are all within one or two degrees of one another. This leads us to believe that the testes do not influence each other much when both are heated simultaneously.

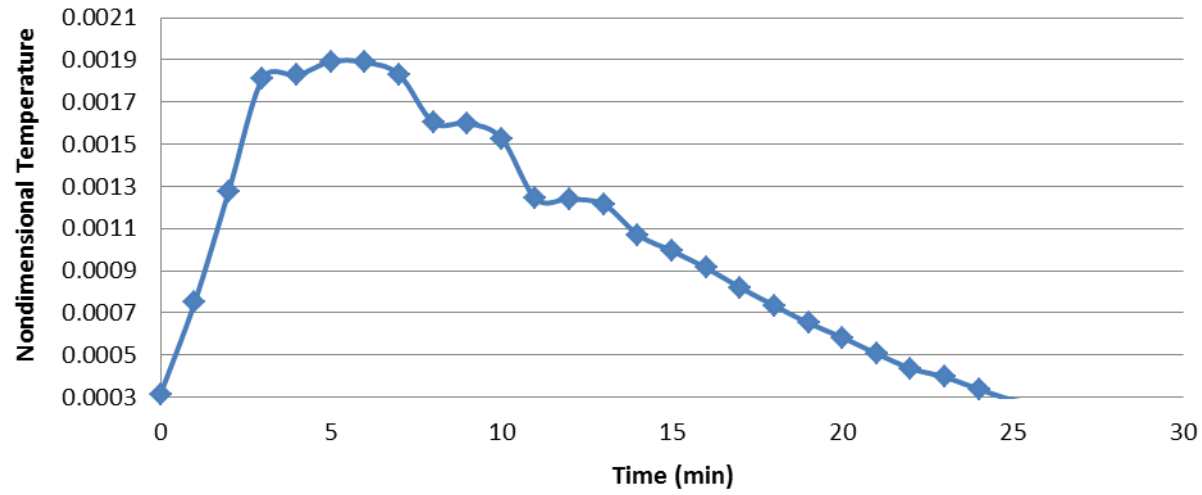

Figure 3.28 Non-dimensional temperature as it approaches steady state for isolated testicle

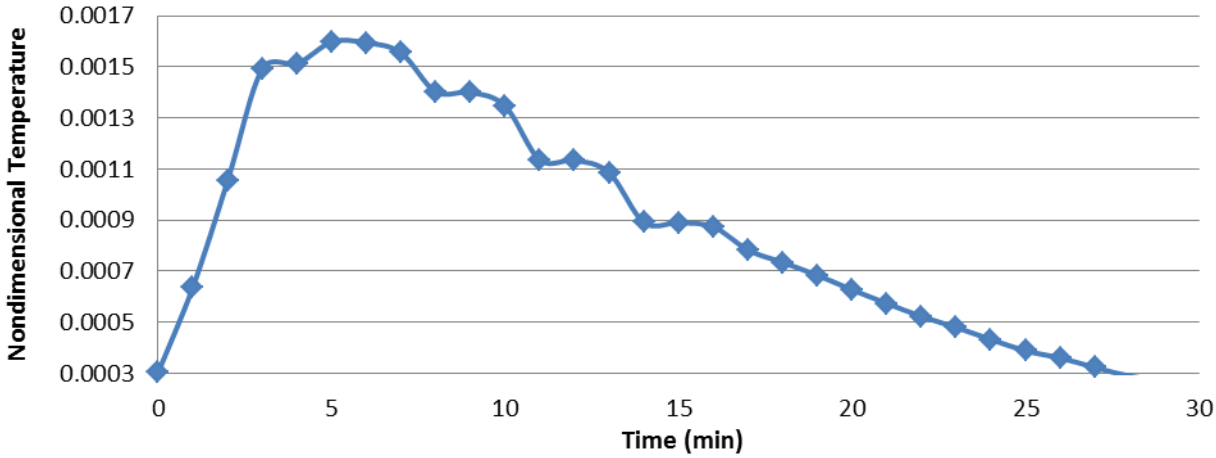

Figure 3.29 Non-dimensional temperature as it approaches steady state for non-isolated testicle

Table 3.2 Average temperature at minute 15

	Instantaneous Temp. @ Minute 15		(5 Minute) Running Average Temp. @ Minute 15		(1 Minute) Running Average Temp. @ Minute 15	
Radius	Isolated	Non-isolated	Isolated	Non-isolated	Isolated	Non-isolated
0	311.7	310.7	310.7	310	308.3	307.8
0.5	312	310.3	311	309.5	308.6	307.6
0.76	312.3	310.2	311.5	309.4	309	307.6

3.5 References

Alireza Zolfaghari and Mehdi Maerefat (2011). Bioheat Transfer, Developments in Heat Transfer, Dr. Marc Aurelio Dos Santos Bernardes (Ed.), ISBN: 978-953-307-569-3,

Department of Health. September 2015. https://www.health.ny.gov/environmental/outdoors/air/smoke_from_fire.htm (accessed July 21, 2016).

González, Fj. 2007. "Thermal Simulation of Breast Tumors." *Revista Mexicana de Física* 53 (4): 323–26. http://www.scielo.org.mx/scielo.php?script=sci_arttext&pid=S0035-001X2007000400014.

Kastelic, J. P., R. B. Cook, G. H. Coulter, and R.G. Saacke. 1996. "Insulating the Scrotal Neck Affects Semen Quality and Scrotal/Testicular Termperature in Bulls." *Theriogenology 45* 1 (96): 935–42. doi:10.1017/CBO9781107415324.004.

Kastelic, J. P., G. H. Coulter, and R. B. Cook. 1995. "Scrotal Surface, Subcutaneous, Intratesticular, and Intraepididymal Temperatures in Bulls." *Theriogenology* 44 (1): 147–52. doi:10.1016/0093-691X(95)00155-2.

My Virtual Medical Centre. May 14, 2015. http://www.myvmc.com/anatomy/anatomy-of-the-testes/#c11 (accessed July 23, 2016).

Sealfon, Andrew, and Adrian Zorgniotto. 2015. "A Theoretical Model of Testis Thermoregulation" 286 (286): 123–35.

Setchell, B P. 1998. "The Parkes Lecture. Heat and the Testis." *Journal of Reproduction and Fertility* 114 (2): 179–94. doi:10.1530/jrf.0.1140179.

St. Louis Urological Surgeons. n.d. http://stlurology.com/default.aspx (accessed July 23, 2016). *StudyBlue.* n.d. https://www.studyblue.com/notes/note/n/male-reproduction-system/deck/4626644 (accessed July 25, 2016).

University of Leeds. n.d. http://www.histology.leeds.ac.uk/male/epidymis.php (accessed July 23, 2016).

Weinbaum, S, and L M Jiji. 1985. "A New Simplified Bioheat Equation for the Effect of Blood Flow on Local Average Tissue Temperature." *Journal of Biomechanical Engineering* 107 (2): 131–39. doi:10.1115/1.3138533.

Wissler, Eugene H. 2012. “50 Years of JAP Pennes ’ 1948 Paper Revisited.” *Journal of Applied Physiology*, 35–41.

Young Men's Health. March 19, 2015. http://youngmenshealthsite.org/guides/puberty/ (accessed July 27, 2016).

4. Future Works

For the first project, "Interception of Smoke from a Forest Canopy," we wanted to test the third possibility that the flow through the duct is too high for realistic modeling of updrafts through the canopy by installing a parallel duct to reduce flow through the filter screens. Unfortunately, this was not implemented during the duration of the project.

For the second project, "Flame Merge Experiment," image processing will be done by AmirHessam Aminfar in order to determine the flame characteristics (height, velocity, area, etc.) through edge detection. This will involve applying an ellipse that best fits the fire to track its general movement as shown in Figure 4.1

Figure 4.1 Image processing of Burn #5 (open burn) using an ellipse that best fit the flame and edge detection to determine flame features.

In the last project, "Examination of Testicular Thermoregulation," the effects of convection will be incorporated into the model of the testicle immersed in a heated water bath and when the water bath is taken away and exposed to air for cooling.